



JOINING  
INNOVATION  
AND EXPERTISE

Research Review  
July 2018

# Contents

Message from the Research Director	4
Research Board	6
Technology Fellows	8
Published Research	10
Richard Weck Award Winner	26
Technical Literature Reviews	50
PhD Studies	54
Current Core Research Programme	62
Contact	64



# Message from the Research Director



*"Each year, half of TWI's Industrial Membership subscriptions are invested in the Core Research Programme"*



Paul Woollin  
Research Director

Each year, half of TWI's Industrial Membership subscriptions are invested in the Core Research Programme (CRP) to develop new technologies and meet the future business needs of our Industrial Members. This equated to £4 million in 2017, with a further £12.5 million of public funded collaborative research, covering a wide range of technologies including welding and joining, surface engineering, materials testing, inspection and integrity assessment technologies. The more fundamental research is carried out by TWI's National Structural Integrity Research Centre (NSIRC), where a cohort of postgraduate students work in areas aligned to TWI's research themes.

Topics for research are identified via a process involving collecting needs, wants and wishes at Industry Sector Panel meetings and in one-to-one conversations with individual Industrial Members, and planning TWI's contributions via gap analyses and technology roadmaps. The overall direction of the CRP is guided by 40 technical experts from Industrial Members and academia who comprise the Research Board.

The CRP's main objective is to develop capabilities, namely experts and facilities, to support the everyday businesses of our Industrial Members and initiating a constant stream of innovation. As a result of this work, TWI is able to address manufacturing and operating problems as they arise, ensuring the safety and reliability of structures while also offering competitive advantage to our Industrial Members.

The work of the CRP is disseminated to industry through workshops, webinars, industry-focussed articles and detailed Industrial Member reports, which are peer reviewed by leading representatives of Industrial Member companies and academics, before being released exclusively to our Membership.

This publication includes a summary of the Industrial Member Reports and Technical Literature Reviews from 2017, alongside the full report that won this year's Richard Weck prize for the best research report.

I hope you find this summary helpful and that it encourages you to suggest new areas of research that we can undertake on your behalf in the future, or to contact us to seek details of our latest technologies.

# Research Board

The Research Board is a committee of representatives from Industrial Member companies. It determines the content and guides the progress of the Core Research Programme.

**Chairman, Research Board:**

Professor John Irven MA, PhD, CSci,  
CChem, FRSC – Consultant

**Chairman, Engineering Committee:**

Professor Bob Ainsworth MA, DPhil, FRS,  
FIMechE, FEng – University of Manchester

**Chairman, Materials Committee:**

Gareth Hopkin MA, CEng – Office for Nuclear Regulation

**Chairman, Joining and Fabrication Committee:**

Dr Ernst Miklos MSc, EWE – Linde Group

Dr Abdulaziz Al-Meshari BSc, PgDip, MSc – Saudi Basic Industries Corporation (SABIC)

Mr Tareq Al-Sabti MSc – Aramco

Dr Rob Backhouse BEng, EngD, FIMMM – Rolls Royce Plc

Julien Banchet BSc, MSc, MA(Hons) – Areva

Dr Carl Boettcher – Rolls-Royce Plc

Martin Bolander – Westinghouse Electric Sweden AB

Marcel Buckley – GKN Aerospace

Professor Gary Coleman – The Boeing Company

Chris Dash BScE(Hons), MS, PE – Conoco Phillips Company

Dr Nabil El Barbari – GF Piping Systems

Dr Fernando Fernandez BSc(Hons) MSc, MBA – Embraer

Sebastien Garnier – Areva

Brett Hemingway – MAI Manufacturing Operations - BAE

Eur Ing Peter Hilton BSc(Hons), CEng – Shell

Robert Holmes – Canadian Nuclear Laboratories

Craig Hunt BSc(Hons) – Air Products Plc

Jimmy Johansson – GKN Aerospace

Shinji Koga – Kawasaki Heavy Industries

Dr Bruno Leduey – Lincoln Electric



Professor Zhiqiang Li – AVIC Beijing Aeronautical  
Dr Mario Macia PhD – ExxonMobil Production Company  
Dr Ian Merchant – Consultant  
David Milliken – The Boeing Company  
Kelly Moran – The Boeing Company  
Roberto Morana – BP Exploration Ltd  
Dr David Panni CEng – J C Bamford Excavators Ltd  
Holly Phillips MRINA, MCMI, MIIMS – RNLI  
Cheryll Pitt BSc(Hons), CEng, FIMMM – Ministry of Defence  
Dr Marcelo Piza Paes MSc, DSc – Petrobras / CENPES / PDEP / TMEC  
Howard Price – BAE Systems  
Javad Safari – TechnipFMC Plc  
Andrew Schofield BSc(Hons) CEng, MIMMM – BAE Systems  
Christopher Thornton MA, CEng, MIMMM SenMWeldI – BP Exploration Ltd  
Naoki Urai – OTC Daihen Europe GmbH  
Jitesh Vaja BScEng(Hons) – AWE Plc  
Darren Wilson – Smith and Nephew UK Ltd  
William Wistance – Lloyd's Register Foundation

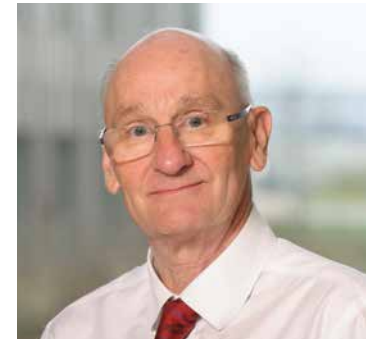
# Technology Fellows

TWI grants the title and role of Technology Fellow to recognised expert staff who epitomise TWI's commitment to the development of world-class technology to solve industrial problems.

Technology Fellows are leading authorities in their technical fields and have international reputations. As well as having made a significant impact on TWI's technology, and consequently the business of our Industrial Members, their day-to-day role includes the development and mentoring of the next generation of experts in their technical field.



Professor Isabel Hadley  
MA, PhD, FWeldI  
*Fracture mechanics and BS7910*



Professor John Wintle MA, MSc,  
CEng, FI MechE, FWeldI, FInstP  
*Integrity management*



Eur Eng Mike Gittos BSc, MSc,  
CEng, MIIMMM, SenMWeldI  
*Metallurgy and failure analysis*



Dr Mike Troughton BSc, PhD,  
CEng, CPhys, MInstP, FWeldI  
*Polymers*



Dr Steve Maddox PhD  
*Fatigue of welded structures  
and components*



Professor Peter Mudge CEng,  
FIMMM, HonFInstNDT, FWeldI  
*Non-destructive testing*



Professor Alan Taylor  
BSc, MSc, PhD  
*Ceramics, coatings and  
nanomaterials*



Dr David Howse BEng, EngD,  
CEng, EWE, MIMMM, FWeldI  
*Arc processes, fabrication  
and welding engineering*



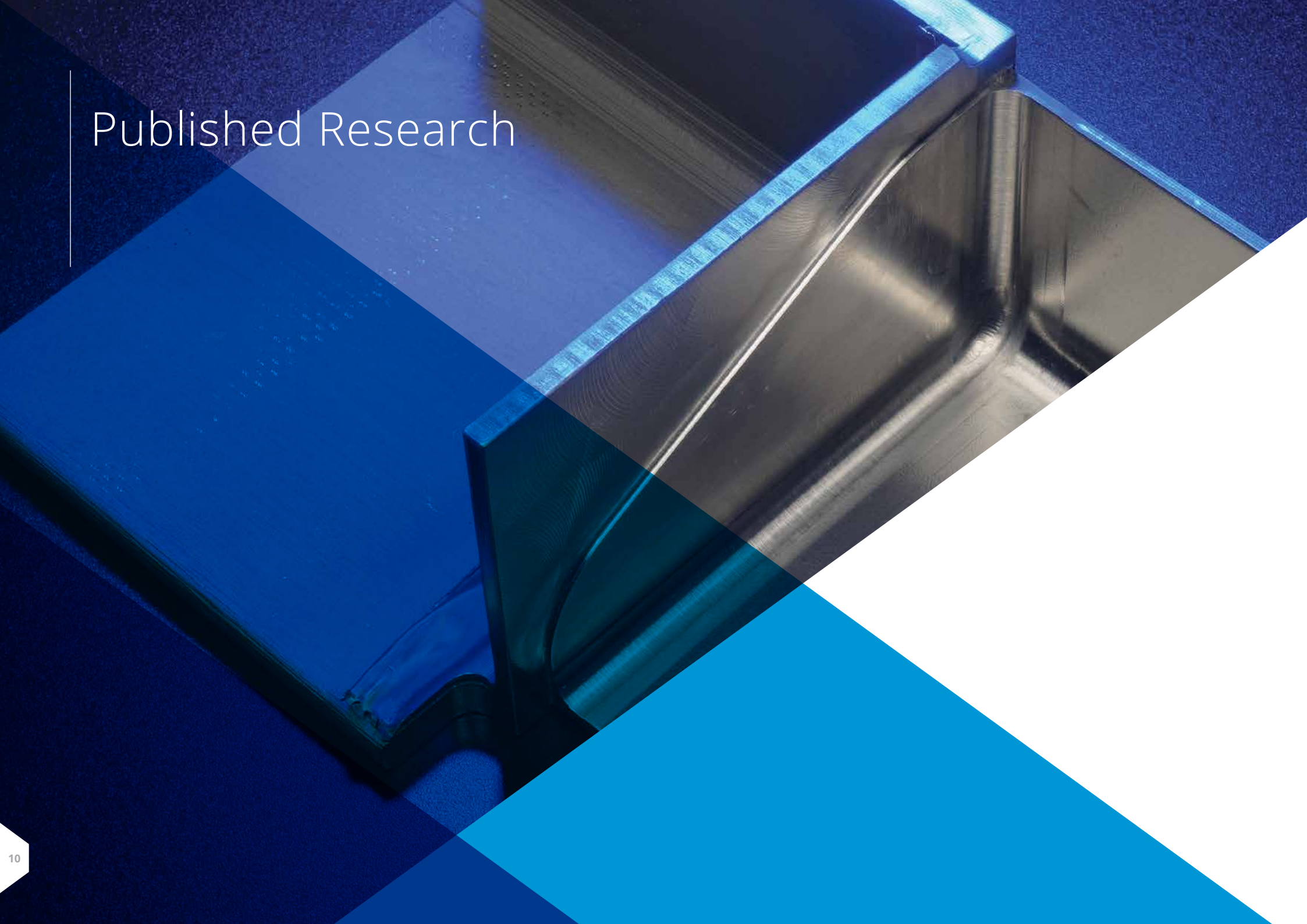
Professor Ian Cooper BSc,  
MSc, CEng, FInstNDT, ASNT  
*Advanced non-destructive testing*



Eur Ing Charles Schneider MA,  
CEng, MWeldI, FInstNDT, MIAQP  
*Non-destructive testing - reliability*



Richard Pargeter MA, CEng,  
EWE, MIMMM FWeldI  
*Sour service and ferritic steel*



# Published Research



## Materials Processing Laser Cutting of Fibre-Reinforced Polymers

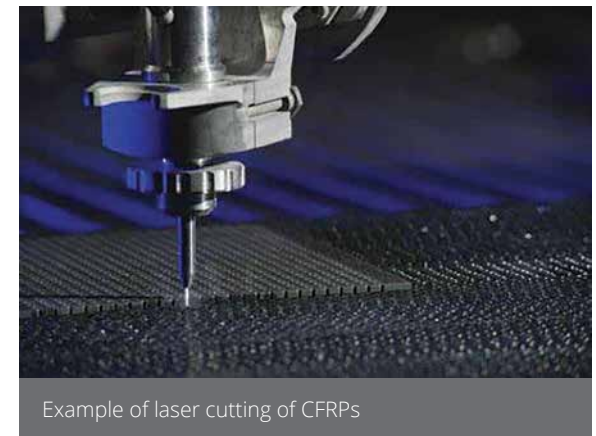
Ian Jones Report 1079

### Background

Laser processing has significant potential for the cutting of fibre reinforced polymers (FRPs), given that it is a non-contact, precise, low heat-input, high-productivity and highly automated process. Currently, however, laser machining of FRPs is not commonly used by industry. This report provides a review of the recent R&D of the processes for laser cutting of FRPs, highlighting the most successful procedures and identifying research needs.

### Key Findings

- Technologies currently employed in cutting composites include milling, abrasive water-jet cutting, electrical discharge machining, ultrasound machining and laser cutting.
- Compared to other methods, laser cutting provides a narrow kerf, a high production rate and automation capability, although it can give thermal damage at the cut edge and produces fume and dust.
- Laser cutting of carbon fibre composites provides greater challenges than glass or aramid fibres.
- Many studies have investigated methods of reducing the thermal damage or heat affected zone (HAZ), whilst retaining a high production rate. To date the most promising results, in terms of cut edge quality, have been seen using high power lasers, with high speed multiple pass scanning methods.
- By comparison, single-pass, gas-assisted laser cutting results in a wider HAZ, but is better suited to long cuts and large parts than a multiple-pass technique.
- Short pulse (picosecond and nanosecond) and UV laser systems provide very good cut edge quality, but slow processing rates.



Example of laser cutting of CFRPs

# Published Research



## Materials Joining

### Advancement of Arc Welding Repair of Mar-M247 and Alloy 713C

Robert Shaw Report 1080

#### Background

Precipitation-strengthened nickel alloys are commonly used for cast components in the aero-engine and power generation industries. The components are of high value, such that their scrappage can have a significant economic impact. Therefore, it is desirable to be able to perform arc weld repairs on these components, particularly in low stress regions in which post-weld heat treatment might be deemed unnecessary.

Precipitation-strengthened nickel alloys have a range of weldability with weld cracking susceptibility being often well correlated with aluminium and titanium content. Alloys containing more than six atomic percent combined aluminium and titanium are generally considered unweldable. This includes alloys which are widely used, like Mar-M247 and Alloy 713C, in which TWI's Industrial Members have expressed an interest.

Previous work on these alloys has shown significant difficulty in performing weld repairs without solidification or liquation cracking, so this body of work was initiated with the intent of investigating process space not yet explored. A literature review was undertaken, 'Shaw, 2013: TWI Technical Literature Review 22954: A Review of Weld Repairs of Mar-M247 and Similar Alloys', which set the direction of this work.



Example of repaired blade



## Materials Processing

### Laser Surface Processing to Alter the Elastic Properties of Nylon-Elastane Fabrics: An Initial Study

Helen Paine and Ian Jones Report 1081

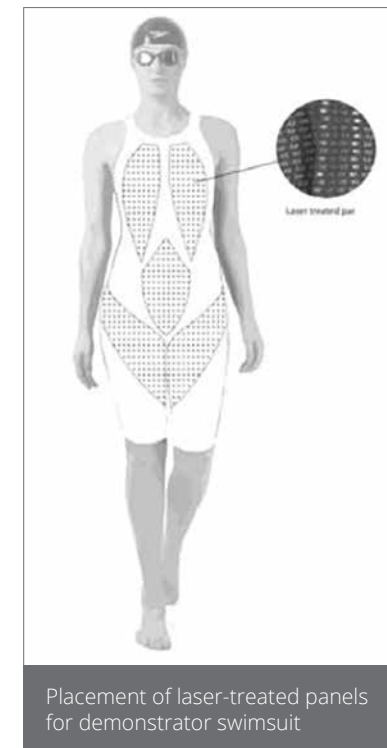
#### Background

The elastic properties of fabrics are important in many applications, including garments for sports training and competition and for medical products, which rely on control of compressive forces over defined locations on the body. Garments with modified elastic properties are used for treatment after surgery and to reduce deep vein thrombosis. Approaches to manufacturing compressive garments include sewing different fabrics together, lamination of additional layers in selected locations, complex weave or knitted patterning and application of patterns of adhesive dots or coatings to the fabric surface. This work aimed to identify the potential for using the laser beam melting method to modify the elastic properties of fabrics. It would allow easy control of the pattern and amount of surface melting, and should be applicable to small or larger areas of the fabrics or garments.

#### Key Findings

Studies into direct diode laser surface treatment of elasticated nylon fabrics, and the effect on the elastic properties of those fabrics has resulted in the following main conclusions:

- Variations in laser processing conditions (power, process speed, and beam spot size) have been shown to demonstrate a controlled effect on the surface of the fabric and the elastic properties. Surface melting and elastic modulus increased at higher heat input processing conditions
- Varying the orientation and the distance between melted lines or using the laser in a pulsed mode allowed control of the elastic properties of the fabric as a whole, including the magnitude and direction of the changes in elastic properties
- Surface melting has a negative effect on the tensile strength of the fabric; however, pulsing and heat input variables have been demonstrated as methods that can be used to mitigate this effect
- Laser beam melted patterns have a significant compressive effect on the surface of the human body; reducing body measurements by 1-2% and increasing pressure values by approximately 60% across all areas tested.



# Published Research



## Structural Assessment

### Fatigue Reassessment of Ageing Pressure Vessels: Life Extension and Change of Use

Emily Hutchison, Emilie Buennagel, John Wintle, Warren Bath and Museok Kwak Report 1082

#### Background

Many ageing pressure vessels were designed with a notional 25-year design life using standards such as BS 1515, which did not require fatigue assessment. This means that the fatigue lives of these vessels have never been calculated. Offshore operators seek a methodology for justifying life extension for vessels designed to older codes through fatigue assessment and a campaign of risk based inspection. Therefore, fatigue assessment is a critical part of the life extension process.

The report outlines the principles for fatigue reassessment of long service pressure vessels and demonstrates these principles by means of a case study on a vessel that has been in service since the 1970s.

#### Key Findings

The case study demonstrated the principle of reassessment based on detailed modelling and inspection of an example vessel. Five necessary phases are:

- Examination of benchmark vessel
- Compliance with standards, including analysis of fatigue loading
- Commonality between vessels
- Engineering critical assessment (if necessary)
- Inspection plan.



Condensate flash separator vessel used for case study



## Materials Processing

### The Effect of Build Strategies and Pre-Heating on the Residual Stress and Mechanical Properties of Selective Laser Melted Ti-6Al-4V Parts

Roger Fairclough Report 1083

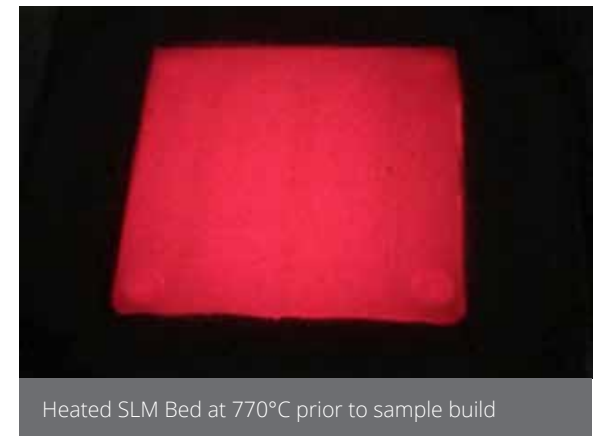
#### Background

Selective laser melting is a manufacturing process with benefits including CAD-to-part capability, high process flexibility and the ability to produce fine intricate features with great accuracy and repeatability. One of the inherent disadvantages of the way the SLM process works, however, is that the repeated heating and cooling during the build cycle creates high temperature gradients, which can lead to the development of high internal (residual) stresses.

Developments to reduce residual stress and consequential component distortion and performance restrictions are of great importance and relevance within industry to increase adoption of the SLM process. Titanium alloy Ti-6Al-4V gr23 was chosen as the candidate material for this work based on its extensive use within the aerospace and biomedical industry sectors and its increasing use in other general engineering applications.

#### Key Findings

- Build strategies were developed that reduce residual stress development whilst still maintaining or improving mechanical properties of Ti-6Al-4V test samples.
- An SLM machine was modified to have a heated bed capable of pre-heating and maintaining a bed temperature of  $> 770^{\circ}\text{C}$ .
- Samples built at  $>470^{\circ}\text{C}$  were shown to exhibit zero residual stress.



# Published Research



## Structural Assessment Assessment Procedures for Non-Sharp (Blunt) Defects

Philippe Bastid, Sabrina Blackwell, Yin Jin Janin, Ruth Sanderson, Guiyi Wu and Isabel Hadley Report 1085

### Background

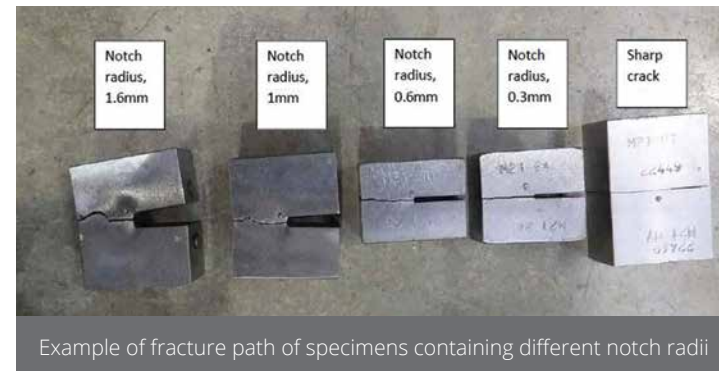
Current engineering critical assessment (ECA) methods treat most flaws as crack-like; ie infinitely sharp at the crack tip. This may be too conservative when the actual flaw is non-sharp. This may lead to inefficient over-design, and unnecessary shutdown, repair, refurbishment or replacement. An assessment technique taking account of non-sharp defects can therefore reduce fabrication and operating costs, and improve safety.

- The threshold stress for propagation of micro cracks to cleavage fracture was identified for parent and weld metal
- Bordet's advanced local approach model is suitable for the prediction of the fracture probability of specimens with various initial crack notch radii, accounting for both the initiation of micro-cracks and their propagation to cleavage fracture.

### Key Findings

A programme of mechanical testing and numerical modelling was carried out with the following outcomes:

- Apparent fracture toughness increases approximately linearly as the notch tip radius increases
- Notch radius affects the brittle-ductile transition temperature. The greater the notch radius, the lower the brittle-ductile transition temperature
- FEA showed that the predicted load-crack mouth opening displacement (CMOD) curve was, in general, slightly under estimated in the case of the parent metal and over-estimated in the case of the weld metal



Example of fracture path of specimens containing different notch radii



## Structural Assessment Material Models for Improved Finite Element Predictions of Residual Stresses in Ferritic Steels

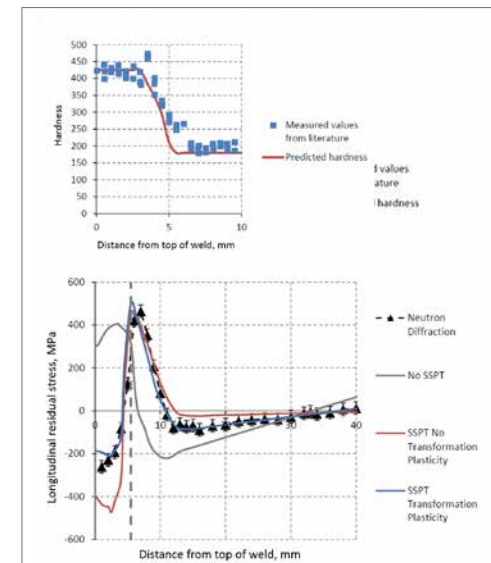
Nicholas O'Meara Report 1086

### Background

Knowledge of welding residual stress is required to ensure welded structures are able to operate with sufficient resistance to certain failure mechanisms. In light of the difficulties associated with measuring residual stresses, finite element simulation can be used to predict stress evolution during welding processes. Solid state phase transformations, as experienced by ferritic steels, can affect residual stress evolution and should be accounted for in modelling approaches in certain cases. In this report, models to incorporate these effects using a widely used finite element modelling package are presented.

### Key Findings

- Predictions of microstructure and residual stress in a ferritic benchmark weld were made and compared with published measurements for this specimen.
- Flexible user subroutines can be written that allow phase transformation behaviour to be accurately simulated in ABAQUS.
- Low alloy steel phase transformations, can significantly affect welding residual stresses;
- Beneficial compressive stresses in the HAZ of ferritic welds, induced by low temperature phase transformations have been simulated.
- It is possible to accurately predict the micro hardness distribution in the weld using calibrated phase transformation models.



Accurate engineering data, such as micro-hardness and residual stresses, can be predicted when microstructural evolution is accounted for in finite element models

# Published Research



## Materials Processing Development and Understanding of Wire-Fed Electron Beam Additive Manufacturing

Anita Ward and Nick Bagshaw Report 1087

### Background

Wire-fed electron beam additive manufacturing (W-EBAM) and other wire additive processes enable a large volume of material to be deposited rapidly, but require a final machining operation to reach final dimensional tolerances. The aerospace community is focussing on these high deposition rate technologies, in a drive to reduce material usage and scrap. However, in order for W-EBAM to provide an industrially viable solution, distortion issues require control.

### Key Findings

- W-EBAM deposits of up to 50mm have been built in Ti-6Al-4V at a rate of 0.5kg/hr.
- A stiffening effect is observed as the height of the deposit increases; however, the rolling direction does not have a significant effect on the distortion of the plate.
- An FEA model of distortion in the W-EBAM process has been developed and validated and used to investigate distortion mitigation strategies. Preheating the substrate provides the best benefit – 45% reduction in distortion.
- Improvements in processing quality were achieved through reducing the processing power as the build height increased.
- A demonstrator aerospace wing rib post was fabricated to promote the process and a zircaloy deposit was made to show the potential for power sector applications.
- Basic calculations suggest a 40% reduction in cost over machining from solid.



Partially-machined, fabricated wing rib post demonstrator



## Structural Assessment

### Residual Stress in Girth Welded Pipeline After High Plastic Deformation

Elvin Eren, Shu-Yan Zhang, Tyler London, Jianxin Gao and Isabel Hadley Report 1088

#### Background

Welding residual stresses can have a profound influence on the fracture and fatigue behaviour of welded joints. Consequently, structural integrity assessment procedures typically include compendia of residual stress distributions for a range of joint types, plus methods for incorporating the effects of residual stress into analyses. They also include advice on circumstances in which residual stresses can be relieved, for example through the use of post-weld heat-treatment or mechanical stress relief.

Residual stresses are modified by high applied strains, as experienced in, for example, pipe reeling operations. Understanding this redistribution will allow greater accuracy in fitness-for-service assessments, potentially improving safety and reducing overdesign.

#### Key Findings

- Narrow gap welded pipe spools exhibited significantly lower axial residual stresses in the as-welded condition than conventionally welded pipes.
- The distribution and the peak value of hoop residual stresses in the girth welded pipe spool were of the order of and exceeding the yield strength of the parent material. This distribution is in line with the profiles available in the codes and standards.
- After the application of 3% remote strain, the hoop component of the residual stress reduced significantly and yield magnitude residual stress in the weld vanished, whereas the far-field hoop residual stresses increased from negative values to values in the order of 100 200MPa.
- In general, both the radial and axial residual stresses decreased. When the distributions after straining are examined, it can be seen that radial and axial residual stresses were negative and followed a stable trend rather than fluctuating in the vicinity of the heat-affected zone or in the far-field.



Measurement of residual strains in the axially strained pipe spool

# Published Research



## Materials Joining

### Automatic Tig Ambient Temperature Temper-Bead Technique for Ni-Based Weld Overlay Repairs of Nuclear Components

Marcello Consonni and Claire Verdon Report 1089

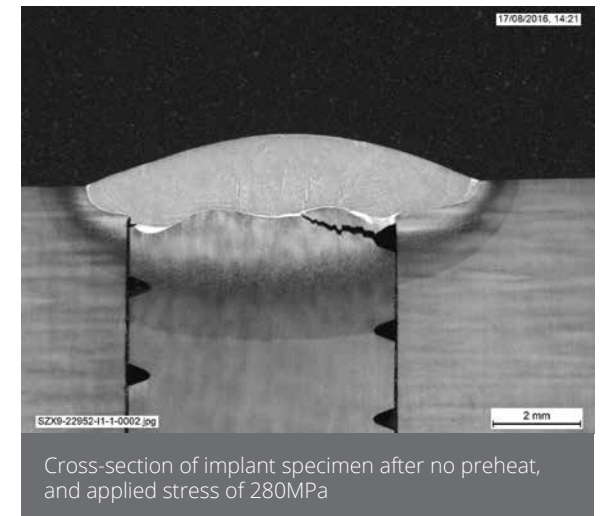
#### Background

Practical challenges may make any heating cycle undesirable when repairing nuclear power plant components by full-strength weld overlays (FSWOLs). So, repair solutions that do not require preheat, PWHT or post-heating, referred to as 'ambient temperature temper bead' (ATTB), have been developed. The ATTB technique is currently permitted for the repair of nuclear power plant components by the ASME code, but it is currently not permitted by the RSE-M code. As the current rules in the RSE-M codes were established following experimental programs based on implant testing, the same type of tests would be expected to justify any changes.

#### Key Findings

A previous programme based on implant testing, described in a technical review of the application of ATTB to nuclear power plant components, failed to justify the introduction in the RSE M code of the ATTB technique for the application of FSWOLs using Ni-based filler metal on nuclear components. The shortcomings of this programme were taken into account to devise the experimental programme described in this report, from which the following can be concluded:

- Implant test results showed that at the residual stress levels predicted for FSWOLs, cracking may occur in ferritic material following the deposition of single weld beads using Ni-based filler metal and without preheat
- A preheat temperature of at least 75°C is required to prevent hydrogen cracking, but only a limited number of specimens could be tested, which is not considered sufficient to confirm a safe condition at this temperature
- Implant test stresses based on residual stresses acting on multilayer FSWOLs may be overly conservative when testing single bead deposits.



Cross-section of implant specimen after no preheat, and applied stress of 280MPa



## Materials Processing Microwave Curing of Composites

M Kwak, T Arampatzis, K Selvaraj  
and Mihalis Kazilas Report 1090

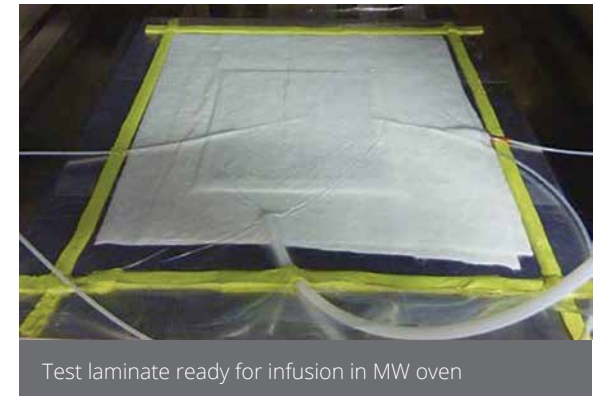
### Background

Composite parts are being used in a wide spectrum of applications, covering markets such as aerospace, automotive, power and medical. Their increased use has given rise to challenges with respect to production rates. New, faster manufacturing processes are needed in order to satisfy the current demand of composite structures. Thermoset cure is inherently a slow process.

Microwave (MW) heating could speed up the cure cycles (typically lasting several hours) with no loss of quality due to the instantaneous heating capability and the energy absorbent nature of carbon fibres at the MW frequency.

### Key Findings

- The axial tensile properties showed little difference between MW and oven cured samples.
- The transverse tensile and in-plane shear (IPS) modulus were lower for the MW cured samples.
- The consistency in test results observed in MW cured composites is an indication of even heating through and across the laminates.
- There is very little difference in the matrix modulus between the MW cured and oven cured samples.
- The selective heating nature of MWs created local variations in matrix ductility, essentially transforming the matrix into a two-phase system with a hard brittle region close to the fibre, and a more ductile and tougher region away from the fibre.



Test laminate ready for infusion in MW oven

# Published Research



## Non-Destructive Testing

### Detection and Characterisation of Stress Corrosion Cracking in Austenitic Weld Overlay Cladding for Non-Intrusive Inspection

Channa Nageswaran Report 1091

#### Background

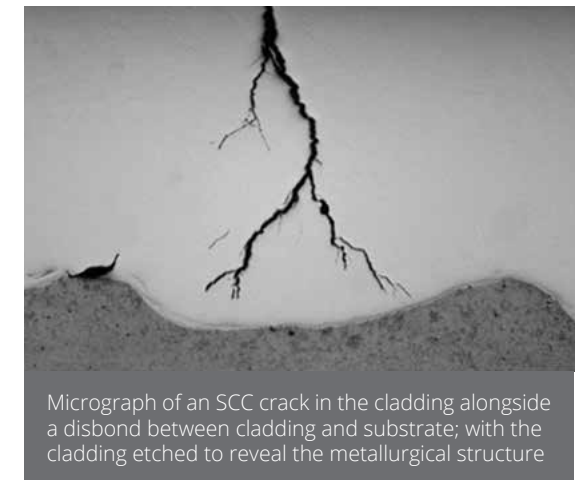
Weld overlay cladding in stainless steel is used in pipelines and processing vessels to protect against corrosive fluids. Stress corrosion cracking (SCC) is a known damage mechanism in these cladding systems and could lead to a catastrophic failure of the component. Hence, detection of SCC at onset and assessment of the size of cracking is a key requirement to allow for safe and effective management of these components.

#### Industrial Challenge

There is a need in industry to inspect the internal clad surfaces of components using non-intrusive inspection (NII) techniques and this project identifies those techniques that could be implemented in NII programmes.

#### Key Findings

- Phased array (PAUT) and post-processing (FMC/TFM) ultrasonic techniques can be implemented from the outside surfaces of vessels and piping to detect and characterise SCC.
- Electromagnetic acoustic transducers (EMATs) and eddy current arrays (ECAs) are effective at detecting SCC when applied from the cladding surface.
- X-ray computed tomography (CT) is also able to characterise SCC with good resolution and establish its full geometry; however CT is very difficult to implement on components in-situ.
- All techniques investigated and found capable for detection and characterisation of SCC in this report were implemented using portable instrumentation, which are readily available in the market.
- TWI has developed a method to artificially create SCC in weld overlay cladding for use in calibrating and setting the sensitivity of the inspection techniques.



Micrograph of an SCC crack in the cladding alongside a disbond between cladding and substrate; with the cladding etched to reveal the metallurgical structure



## Materials Joining

### Effect of Back Purging Gas Oxygen Content on Weld Discolouration and Corrosion Resistance of Autogenous Tungsten Inert Gas Welds in Duplex Stainless Steel Pipes

Usani Ofem Report 1092

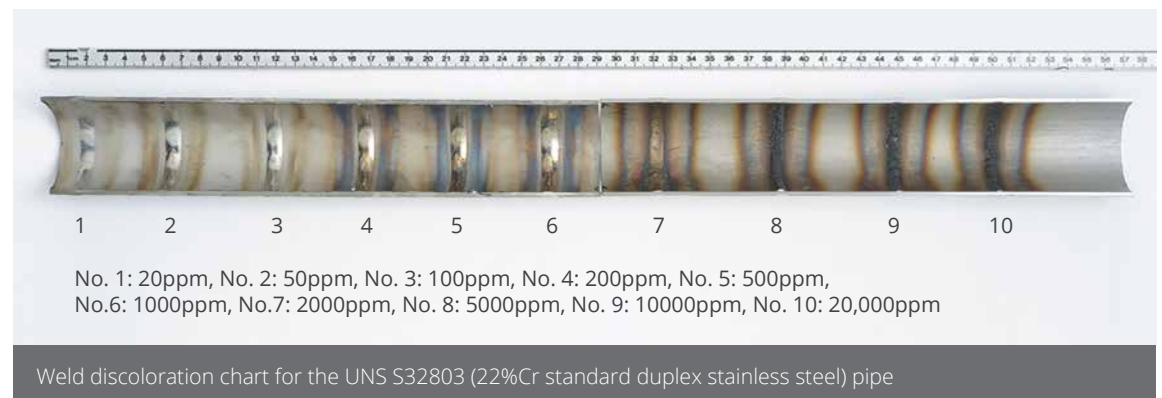
#### Background

Composite parts are being used in a wide spectrum of applications, covering markets such as aerospace, automotive, power and medical. Their increased use has given rise to challenges with respect to production rates. New, faster manufacturing processes are needed in order to satisfy the current demand for composite structures. Thermoset cure is inherently a slow process.

Microwave (MW) heating could speed up the cure cycles (typically lasting several hours) with no loss of quality due to the instantaneous heating capability and the energy absorbent nature of carbon fibres at the MW frequency.

#### Key Findings

- The axial tensile properties showed little difference between MW and oven cured samples.
- The transverse tensile and in-plane shear (IPS) modulus were lower for the MW cured samples.
- The consistency in test results observed in MW cured composites is an indication of even heating through and across the laminates.
- There is very little difference in the matrix modulus between the MW cured and oven cured samples.
- The selective heating nature of MWs created local variations in matrix ductility, essentially transforming the matrix into a two-phase system with a hard brittle region close to the fibre, and a more ductile and tougher region away from the fibre.



# Published Research



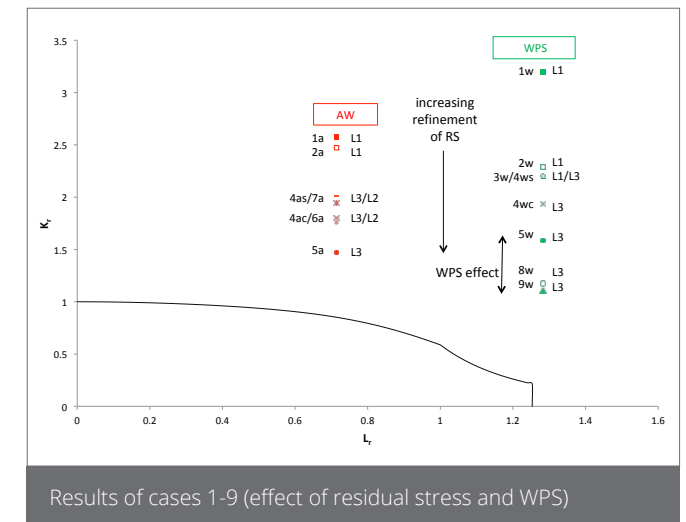
## Structural Assessment Effects of Warm Pre-Stress on Residual Stress and Fracture in Uniaxially Loaded Welded Joints Isabel Hadley Report 1093

### Background

TWI's fracture test database includes details of an extensive programme of wide plate tests on both plain steel plates and welded joints, with and without application of a warm pre-stress (WPS). The R6 and BS 7910 fracture assessment procedures have developed since the tests were carried out, and the results provide an opportunity to validate various aspects of both procedures; not only the treatment of welding residual stress, but also the enhancement of fracture toughness due to WPS, the effect of weld strength overmatch and the treatment of plastic collapse.

### Key Findings

- The transverse residual stress data for a butt-welded joint in a ferritic steel weld are reasonably represented by the upper bound curves given in BS 7910 and R6.
- The model for the enhancement of apparent fracture toughness after a WPS event is consistent with experimental results.
- Refinement of the treatment of residual stress from a simple Level 1 approach to a Level 3 approach allowed an almost threefold reduction in the value of  $K_r$  at failure.
- The initial estimate of  $L_r$  was reduced by a factor of around 1.3 once a revised global limit load solution was used, and the effects of mismatch taken into account.
- To date, all of the results associated with failure of the plate lie outside the default failure assessment line (FAL), so they support the fracture models in BS 7910 and R6.





## Structural Assessment Effects of Biaxiality on Residual Stress Relief and Fracture in Welded Joints

Isabel Hadley Report 1094

### Background

TWI's database of full-scale fracture tests includes wide plate tests carried out on well characterised welded joints with and without use of a warm pre-stress (WPS). This work relates to a set of tests carried out at  $-70^{\circ}\text{C}$  on surface cracked specimens using biaxial loading conditions for both the WPS (where applicable) and the final failure condition. Factors other than this (weld procedure, flaw size, materials properties, etc) were matched as far as possible in order to ensure that WPS was the only significant variable between the tests. The main objectives were to:

- Demonstrate the effect of WPS under different biaxiality conditions on welding residual stress
- Calculate the effect of biaxiality on failure in terms of fracture assessment procedures
- Analyse the effect of biaxiality on the relief of welding residual stresses during WPS, and compare these results with experimental measurements
- Demonstrate the effect of using different reference stress/limit load solutions on failure assessment.

### Key Findings

- Residual stresses transverse to the weld in an uncracked joint subjected to a simulated WPS were higher when biaxial loading was applied than under uniaxial loading conditions; ie there was less mechanical relief of residual stresses under biaxial conditions.
- The initial estimate of  $L_r$  was reduced by a factor of around 1.3 once a revised global limit load solution was used, and the effects of biaxiality had been taken into account.
- Refinement of the treatment of residual stress from a simple Level 1 approach to a Level 3 approach allowed a reduction in the value of  $K_r$  at failure by a factor of around two.
- All the results associated with failure of the biaxial wide plates lie outside the default failure assessment line, so can be considered to support the fracture models in BS 7910 and R6.
- The Level 1 model for residual stress relaxation is a reasonable representation of the data obtained after WPS, especially if the appropriate plastic collapse model is used and weld strength mismatch and biaxiality are taken into account.
- The experimental data used to validate the BS 7910 plastic collapse equations, when analysed in terms of the R6 global collapse model, produce several points on the 'unsafe' side of the boundary; ie the equations overpredict the observed failure load.

# Richard Weck Award Winner

The Welding Institute's Richard Weck Award is given annually for the worthiest Industrial Member report from the Core Research Programme. The award is named after Richard Weck, a former Director General of BWRA and The Welding Institute.

## Nomenclature

B: wall thickness.

ECA: engineering critical assessment.

Hi-lo: the offset between the inner pipe surfaces on each side of the weld.

FE: finite element.

$M_k$ : a magnification factor to account for the effect of the stress concentration factor at the weld toe on  $\Delta K$ .

SCF: stress concentration factor.

SCR: steel catenary riser.

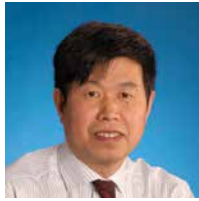
**Type I defect model:** the weld root bead profile is symmetric about the weld centre line and the wall thicknesses of the pipes either side of the weld are the same ( $hi-lo=0$ ).

**Type II defect model:** the geometry is essentially two pipes with the same outer diameter but different wall thickness, and the weld root is flush with the inner surface of the pipe with larger wall thickness ( $WRBH=hi-lo$ ).

**Type III defect model:** the geometry is that of two pipes with the same outer diameter and different wall thicknesses joined by a weld with the weld root bead extending beyond the inner surface of both pipes ( $WRBH \neq hi-lo$ ).

WRBW or w: weld root bead width.

WRBH or h: weld root bead height.



## Developing $M_k$ Solutions for Fatigue Crack Growth Assessment of Flaws at Weld Root Toes in Girth Welds

Yan-Hui Zhang, Tyler London and Damaso De Bono

Report 1084

### 1 Introduction

For single-sided girth welds in pipelines and risers, the fatigue design codes define a higher class S-N curve for the weld cap (Class D according to BS 7608:2014) than for the weld root (Class E) to account for the effect of possible poor weld root profile on fatigue performance. Indeed, fatigue cracking is often found to initiate from weld toes on the root side, rather than on the weld cap side, during full-scale fatigue testing of girth welded pipes as shown in Figure 1 (Zhang and Maddox, 2014). The weld shown in Figure 1 in this case was made with a copper backing shoe on the inside surface as is sometimes used in the production of girth welds. Compared with the profile at the weld cap, the weld root exhibits two distinctive features: a sharp surface discontinuity and a much smaller weld width. In the examples shown in Figure 1, there was a step between the weld root and the neighbouring pipe surface. The fatigue crack initiated from the corner where there was a stress concentration factor (SCF).

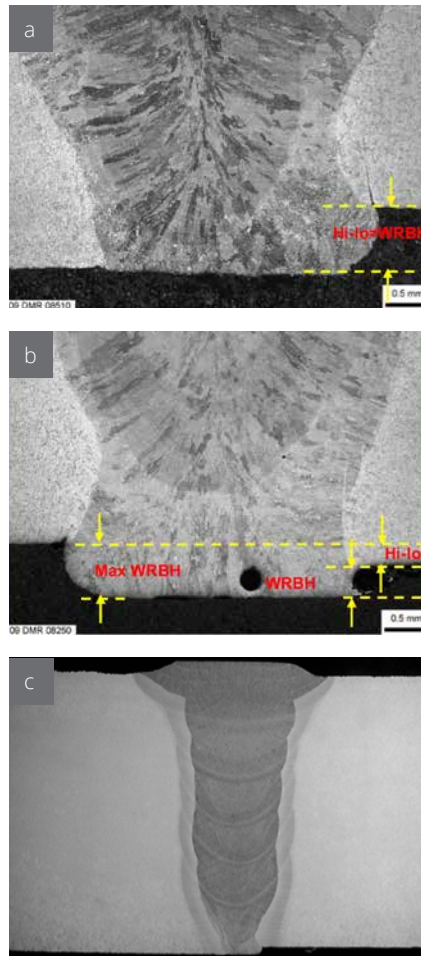


Figure 1 Examples of weld profiles of single-sided girth welds made with copper backing:  
a) Weld root bead profile, with the hi-lo identical to WRBH;  
b) Weld root bead profile, with the hi-lo less than the maximum WRBH;  
c) Weld profile for a whole girth weld, showing a much smaller weld width at the weld root than at the weld cap.

For welded joints, fatigue life is dominated by the crack propagation process because crack-like flaws are unavoidably introduced (Maddox, 1991). Metallography conducted on “sound” welds indicates that they contain undercut and intrusions at the weld toe in the range 0.15mm to 0.4mm deep and approximately 2mm long (Signes et al, 1967). Thus, fracture mechanics can be used to characterise the fatigue behaviour of welded joints. Fatigue crack growth rate ( $da/dN$ ) can be described by the Paris power law which shows the relationship between crack growth rate and stress intensity factor range,  $\Delta K$ , which is a function of crack size and stress range. To account for the effect of the SCF at the weld toe on  $\Delta K$ , a magnification factor,  $M_k$ , has been proposed (Maddox and Andrews, 1990):

$$1 \quad M_k = K_{in} \text{ plate with weld} / K_{in} \text{ plate without weld}$$

$M_k$  quantifies the change in stress intensity factor as a result of the presence of the surface discontinuity at the weld toe.  $M_k$  increases with increasing weld width  $w$  and decreases sharply with increasing distance from the weld toe in the thickness direction and usually reaches unity at crack depths of typically 30% of wall thickness.  $M_k$  solutions have been generated for cracks at the toes of welds (eg, Smith and Hurworth, 1984; Maddox and Andrews, 1990; Bowness and Lee, 2002). They were derived from finite element (FE) models for butt and T-butt joints.

Although both the two-dimensional (2D) and three-dimensional (3D)  $M_k$  solutions are provided in BS 7910 (2013) for engineering critical assessment (ECA), they are representative of the geometry for the weld cap and do not capture the typical geometry at the weld root seen in Figure 1. Furthermore, use of these  $M_k$  solutions predicts failure at the weld cap, rather than at the weld root, due to under-estimation of the  $M_k$  value at the latter. This is because

of a smaller weld width  $w$  and lower applied stresses on the inner surface under an applied bending moment. The importance of this issue to industry is further highlighted by the frequent revisions in DNV F101 (2010, 2012, 2013) with regard to ECA of a postulated crack at the weld root:

- The 2010 version did not provide specific guidance on how to assess a flaw at the weld root toe;
- The 2012 version provided guidance on assessing flaws at both the weld cap and root. For the latter, it specified setting the weld width  $w$  equal to that at the weld cap but excluding the misalignment-induced SCF;
- The 2013 (current) version specifies setting  $w$  equal to the weld width on the weld root side and multiplying the nominal stress ranges by the misalignment-induced SCF. However, it is not clear whether this guidance is based on numerical modelling.

Therefore, there is a clear need to develop an  $M_k$  solution specifically for assessing defects at the root of girth welds, which the present work aimed to do. Due to the complexity of 3D analyses, it was based on a 2D FE model, which proves to be a conservative approach for flaws of a finite length, and is correct in the case of a straight-fronted crack ( $a/2c=0$ ).

## 2 Objectives

- Develop a 2D  $M_k$  solution specifically for ECA of a flaw at a girth weld root toe;
- Assess the accuracy of the  $M_k$  solution developed using experimental data;
- Examine the suitability of the guidance given in standards with respect to use of  $M_k$  for assessing a flaw at girth weld root toes.

## 3 Brief Review of the $M_k$ Solutions Given in BS 7910

The 2D  $M_k$  solution given in BS 7910 is based on the study by Maddox and Andrews (1990) where a range of cruciform and butt weld geometries in plate was investigated, including different weld bead width to plate thickness ratio,  $w/B$ , weld overfill height ( $h$ ) to plate thickness ratio  $h/B$  and angle between joined plates  $\alpha$ . In all of their models, the top and the bottom parts were symmetrical around the mid-wall thickness. Figure 2a shows the butt welded geometry. The  $h/B$  and  $w/B$  ratios analysed were 0.1-0.2 and 0.5-1.0 respectively. As the plate thickness was 50mm, the minimum  $h$  and  $w$  values investigated were 5 and 25mm respectively. Based on the results of the FE modelling, they concluded that  $M_k$  depends strongly on the ratio of weld width to plate thickness,  $l/T$  in Figure 2a, and that the relative height of the weld overfill or welded attachment,  $h/T$  in Figure 2a does not have a significant effect on  $M_k$ .

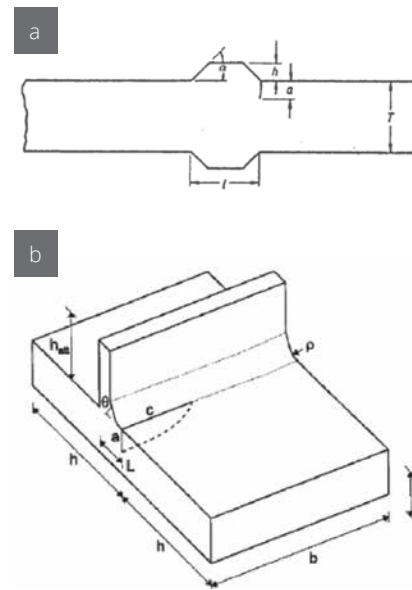


Figure 2 The models investigated (note the different definitions of the weld width in the two models:  $L$  in the 2D model and  $2L$  in the 3D model):  
a) The 2-D butt welded joint geometry analysed by Maddox and Andrews (1990);  
b) The 3-D half T-butt joint geometry analysed by Bowness and Lee (2002).

The 3D  $M_k$  solution given in BS 7910 is based on the work by Bowness and Lee (2002) where  $M_k$  values for semi-elliptical cracks in T-butt welds, Figure 2b, were determined using 3D FE models. A series of parameters were investigated including loading modes (membrane and bending), crack size, crack aspect ratio,  $a/c$  (crack depth over half crack length), weld angle, weld width ( $2L$  in Figure 2b) and

weld toe radius,  $\rho$ . The minimum ratio of weld width over plate thickness,  $w/B$ , investigated was 1.0 and the effect of attachment height was not investigated. It has been verified that the 3D  $M_k$  solution provides a more accurate (less conservative) prediction of fatigue crack growth than the 2D solution (Zhang et al, 2002). However, the 3D solution was developed within certain geometrical limits:  $0.05 \leq a/B \leq 1$ ;  $0.1 \leq a/c \leq 1$  and  $0.5 \leq w/B \leq 2.75$ . For example, for  $B=20\text{mm}$ , the crack depth must be  $\geq 0.1\text{mm}$  and the weld width  $w$  must be  $\geq 10\text{mm}$ . Beyond these limits, the 3D  $M_k$  solution should not be used, and the 2D  $M_k$  solution is recommended instead.

## 4 Finite Element Modelling

### 4.1 Background

For a crack, with a depth of  $a$ , in a structure, the stress intensity factor for mode I is:

$$KI = Y\sigma\sqrt{\pi a}$$

Where  $\sigma$  is applied stress and  $Y$  is a correction factor depending on loading, geometry, crack size and crack front shape. To account for the effect of the SCF at the weld toe,  $Y$  also includes  $M_k$ .

Parametric FE modelling was undertaken to generate and analyse over 6,000 axisymmetric FE models of pipelines containing fully-circumferential, inner surface defects at the toe of an idealised

representation of a girth weld root bead. The parametric study was used to determine the influence of the weld root bead profile geometry on the stress intensity factors for a range of defect depths subject to a remote axial (membrane) stress.

#### 4.2 Software

All FE models were generated using Abaqus/CAE v6.14 and solved using the general static solver, Abaqus/Standard v6.14. Once the modelling approach had been verified on several test geometries, the model generation and analysis processes were automated by developing a Python script that interacted with the Abaqus environment.

#### 4.3 Geometry

The geometry of each model comprised an axisymmetric slice of two lengths of pipe joined by a girth weld. The outer diameter of the pipe was fixed at 406.4mm (16in), and the nominal wall thickness was  $B = 20\text{mm}$ . The total axial length of pipeline modelled was four outer diameters, or approximately 1600mm. The weld itself was assumed to have a flush ground weld cap on the outer surface and only the idealised geometry of the weld root bead on the inner surface was considered.

The weld root bead profile was uniquely characterised by five variables (see Figure 3):

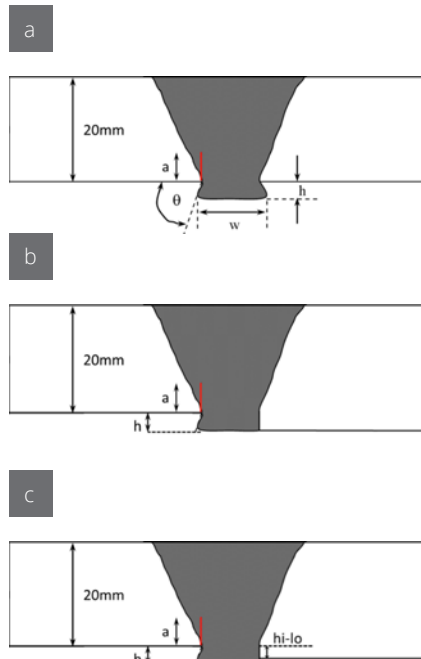


**Figure 3** Illustration of the geometries modelled:  
a) Type I model: weld root  $hi-lo=0$ . In this model, the two lengths of pipe have the same wall thickness;  
b) Type II model:  $hi-lo=h$  (WRBH). The two lengths of pipe have different wall thickness, but the weld root bead is flush with the inner surface of the pipe with the larger wall thickness;  
c) Type III model:  $hi-lo \neq h$ . The two lengths of pipe have different wall thicknesses.

1. Weld root bead width. The weld root bead width  $w$  was defined to be the length (in the axial direction) of excess weld material on the inner surface of the pipe model. Throughout

this report, the weld root bead width is referred to as the weld width or WRBW and is indicated by the variable  $w$ . The resulting parametric  $M_k$  factor solutions were derived in terms of non-dimensional geometric variables, and therefore the weld root bead width was normalised by the wall thickness,  $B = 20\text{mm}$ . The non-dimensional weld root bead width is referenced with an overbar,  $w=w/B$ .

2. Weld root bead height. The weld root bead height  $h$  was defined as the distance between the inner surface and the root of the excess weld. The  $h$  values on each side of the weld can be different, for example, it is almost zero on the left hand side of the weld in Figure 1a. Throughout this report, the weld root bead height is referred to as the weld height or WRBH and is indicated by the variable  $h$ . The non dimensional version of the weld root bead height is also indicated by an overbar,  $h=h/B$ .

3. Hi-lo. Hi-lo is defined as the relative distance between the inner surfaces of the pipe on each side of the weld, Figure 3c. In this study, hi-lo was a measure of the axial misalignment induced by joining pipes with different wall thickness.

4. Weld root bead angle. The weld root bead angle,  $\theta$ , characterises the angle of the weld face as measured from the inner surface of the pipe, Figure 3a.

5. Weld root bead radius. In linear elasticity, a geometrically-sharp, re-entrant corner feature such as a weld

toe generates a stress singularity. A consequence of this is that as the FE mesh is refined in the vicinity of the stress raiser, the solution will not converge; that is, the calculated stress at the weld toe will increase without bound as the local element size decreases. Nevertheless, this peak stress decays rapidly. To overcome this numerical problem, the FE models incorporated a 0.05mm radius into the transition between the inner surface of the pipe and the weld root bead profile. The radius size of 0.05mm was selected because it was smaller than the smallest defect depth considered (0.07mm) and a preliminary sensitivity study indicated that it was a suitable choice for the determination of conservative  $M_k$  factors.

#### 4.4 Models of weld root bead profile

Three distinct models were analysed to characterise different weld root bead profiles:

**Type I model:** the weld root bead profile is symmetric about the weld centre line. An illustration of a Type I model is shown in Figure 3a. All of the geometry cases analysed during the parametric study are listed in Table 1;

**Type II model:** the geometry is essentially two pipes with the same outer diameter but different wall thickness (and the weld root flush with the inner surface of the pipe with the larger wall thickness). An illustration of a Type II model is shown in Figure 3b. The Type II model parametric study used the same values of parameters shown in Table 1 except that the values of weld root bead height were excluded;

**Type III model:** the geometry is that of two pipes with the same outer diameter and different wall thicknesses joined by a weld with the weld root bead extending beyond the inner surface of both pipes. An illustration of a Type III model is shown in Figure 3c.

As outlined in Table 1, only the defect depth, weld root bead width and weld root bead height were varied for the final parametric study, while the weld root bead radius and the weld root bead angle were held constant. This was done because a preliminary sensitivity study showed that the angle and root radius had only a weak influence on the

Table 1 Description of the geometry cases analysed for the Type I defect model.

Pipe outer diameter, OD (mm)	406.4
Pipe outer diameter, OD (in)	16.0
Nominal wall thickness, B (mm)	20.0
Weld root bead angle, $\alpha$ (deg)	90.0 [constant for all analyses]
Weld root bead radius, $\rho$ (mm)	0.05 [constant for all analyses]
Total number of defect depths	20
Total number of WRBW values	12
Total number of WRBH values	15
Total number of simulations	3,600

Defect depth, a (mm)	Log-normalised defect depth, $\log_{10}(a/B)$	Weld root bead width, w (mm)	Normalised WRBW, w/B	Weld root bead height, h (mm)	Normalised WRBH, h/B
0.0700	-2.4559	2	0.1	0.25	0.0125
0.0853	-2.3701	3	0.15	0.375	0.01875
0.1040	-2.2840	4	0.2	0.500	0.025
0.1267	-2.1983	5	0.25	0.625	0.03125
0.1544	-2.1124	6	0.3	0.750	0.0375
0.1882	-2.0264	7	0.35	0.875	0.04375
0.2293	-1.9406	8	0.4	1.000	0.05
0.2795	-1.8546	9	0.45	1.25	0.0625
0.3406	-1.7688	10	0.5	1.5	0.075
0.4151	-1.6829	12	0.6	1.75	0.0875
0.5059	-1.5970	14	0.7	2	0.1
0.6165	-1.5111	16	0.8	2.5	0.125
0.7514	-1.4252			3	0.15
0.9157	-1.3393			4	0.2
1.1159	-1.2534			5	0.25
1.3600	-1.1675				
1.6574	-1.0816				
2.0199	-0.9957				
2.4616	-0.9098				
3.0000	-0.8239				

solution (see Section 5.1). This enabled the parametric study to focus on the variation of a smaller set of parameters.

Note that in Table 1, the values of defect depth are logarithmically spaced between the smallest defect depth, 0.07mm, and the largest defect depth, 3.0mm. This distribution of discrete depth values was chosen because, based on the previous work of Maddox and Andrews (1990), it was observed that the  $M_k$  factor varies with the logarithm of the defect depth (or more specifically, the logarithm of the normalised defect depth). Therefore, since interpolation and surface fitting are best suited for data that is equally spaced, it was decided to use 20 different defect depths for which the log-normalised values were equally spaced between the smallest and largest values.

For all models, the usual axisymmetric coordinate system was used with the axis of the cylindrical geometry aligned with the global Cartesian y-axis, and the radial direction corresponding to the global Cartesian x-axis. For convenience, the crack plane was located at the position  $y = 0$ .

The original work by Maddox and Andrews (1990) considered 2D plane strain representations of butt welds and cruciform joints. A key aspect of their work was that, in the absence of any crack-like defects, the neutral axis was constant throughout the length of the geometry. As a consequence, no additional bending was generated by the application of a remote tensile

force that was aligned with the neutral axis. The geometry considered in this work focuses on the effect of the weld root bead profile and assumes that the weld cap is ground flush. If the Type I model considered in this work was to have been analysed using the same kinematic representation (ie plane strain or plane stress) as the Maddox and Andrews work, then a global bending moment would have been generated due to the shift in the neutral axis in the weld region, and the calculated  $M_k$  factor would have been influenced not just by the geometry of the weld root bead width and height, but also by the additional, misalignment induced bending stress. In contrast to the Type I model, for the Type II and III models, a secondary bending stress is present due to the mismatched wall thicknesses either side of the weld region. Therefore, the new solutions described in this report are specifically for cylindrical bodies with an inner surface defect. If the Type I solutions are to be used for plate-type structures, then an additional misalignment SCF should be included to account for any secondary bending that might occur.

#### 4.5 Finite element mesh

Each model was meshed entirely with 8-node, biquadratic, axisymmetric quadrilateral elements with reduced integration (type CAX8R in Abaqus). The geometry of the part was partitioned in a way that facilitated a highly-refined mesh in the vicinity of the weld root bead geometry and crack whilst permitting a coarser far-field mesh where the stress

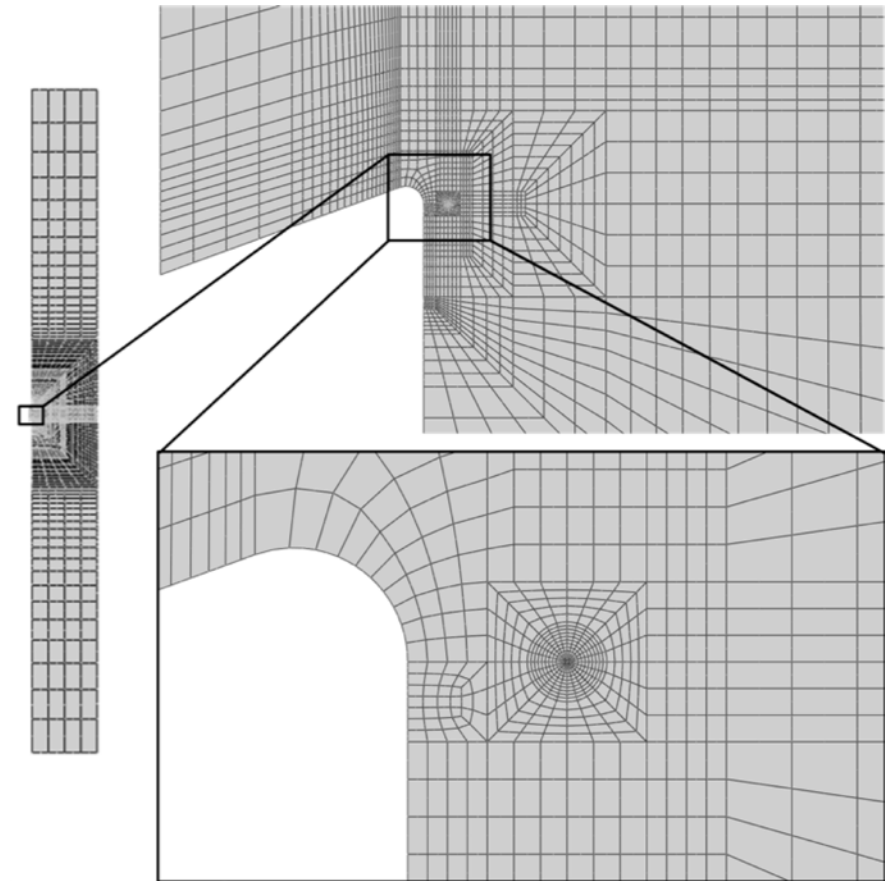


Figure 4 Typical FE mesh for the axisymmetric  $M_k$  factor model.

gradients were significantly reduced. The crack was modelled as a sharp crack, and the crack tip was meshed using a conventional radial spider web mesh comprised of concentric rings of elements surrounding the crack tip. In each model, up to 10 concentric rings of elements were generated around the crack tip and each ring contained between 24 and

48 elements. The innermost ring of elements was comprised of collapsed wedge elements with the mid-side nodes shifted to the quarter point position and single-node degeneracy specified to accurately resolve the  $1/\sqrt{r}$  linear elastic strain singularity. The mesh gradually transitioned from highly-refined to a coarser global mesh. Depending on the local

weld root bead profile geometry, the global part typically contained 6-8 elements through the wall thickness. A typical FE model used in this study is shown in Figure 4.

#### 4.6 Material properties

Since the work was focused mainly on the calculation of stress intensity factors, only linear elastic material properties were considered. Both the lengths of pipe and weld were assumed to comprise of the same homogeneous, isotropic, linear elastic material. The Young's modulus was assumed to be 205GPa and the Poisson's ratio to be 0.3.

#### 4.7 Loads and boundary conditions

The objective of each simulation was to evaluate the stress intensity factor for a specific inner surface defect subject to a remote membrane stress. Because the stress intensity factor varies linearly with applied loads, a remote 1MPa tensile membrane stress was applied by prescribing a suitable concentrated force at a reference node located on the pipe axis at the end of the pipe geometry in the negative y-direction. This reference node was kinematically coupled to the end of the pipe to distribute the concentrated load amongst the FE mesh nodes. The opposite end of the pipe was restrained in the y-direction. All degrees of freedom except for the displacements in the axial direction (U2) were restrained at the reference node. All simulations were analysed under the small strain assumption.

#### 4.8 Post-processing

From each simulation, the stress intensity factor, K<sub>I</sub><sup>FEA</sup> was calculated by Abaqus using an interaction integral method. The stress intensity factor was evaluated along 10 contours surrounding the crack tip and path independence was verified. The value obtained from the outermost contour was then used to calculate the stress intensity magnification factor, M<sub>k</sub>.

For each simulation, the M<sub>k</sub> factor obtained from FEA (M<sub>k</sub><sup>FEA</sup>) was calculated as<sup>1</sup>:

$$3 \quad M_k^{FEA} = K_I^{FEA} / K_I \text{ (BS 7910, flat plate)}$$

The BS 7910 K solution corresponds to the stress intensity factor for a flat plate with a long surface flaw (M.4.2 in BS 7910:2013) having the same wall thickness (20mm), defect depth and applied remote stress (1MPa membrane stress) as the FE model. In this way, the M<sub>k</sub><sup>FEA</sup> factor can be used to directly recover the FEA results, since upon re-arranging Equation [3]:

$$4 \quad K_I^{FEA} = M_k^{FEA} \times K_I \text{ (BS 7910, flat plate)}$$

To be conservative, if M<sub>k</sub><sup>FEA</sup> was calculated to be less than 1.0 then the value was amended and assigned the value 1.0. The interpretation of a case where M<sub>k</sub><sup>FEA</sup> = 1.0 is that the stress intensity factor is no longer affected by the weld toe SCF and equals the value predicted using the handbook solution from BS 7910; therefore,

the interpretation of a case where M<sub>k</sub><sup>FEA</sup> < 1.0 is that, for the given defect depth, the weld toe SCF no longer affects the stress intensity factor, and the stress intensity factor given by the BS 7910 flat plate solution is higher than the FEA axisymmetric stress intensity factor solution. This occurred for only a few cases where the defect depth was in excess of 10% of the wall thickness and is therefore considered insignificant.

#### 4.9 Finite element model automation

Due to the need to understand the variation of stress intensity factors for a wide range of geometry parameters and defect depths, a series of automation scripts was developed in the Python programming language, since Abaqus allows for Python scripts to interact with both the Abaqus/CAE and Abaqus/Viewer environments. There were two primary scripts:

**CreateMkModel.py:** This script was used to create an axisymmetric model of a weld root bead defect given pre-defined geometry variables. The script reads in all of the geometry variables from a structured text file and then calls the Abaqus/CAE environment using the 'noGUI' option so that the script can be run in the background without the need for the user to interact in any interface. The script created the model, partitioned the geometry, assigned material properties, established the analysis steps, meshed the geometry and then wrote the input file. The meshing was defined through a series of

detailed parametric rules that took into account the geometry of the weld root bead profile and the defect height. A feature of this was that for very shallow defects, the meshing was exceptionally dense due to the need to accurately resolve the interaction of the weld root bead profile on the crack tip stress field.

**SubmitAll.py:** This script was the 'master' script for the parametric study. In this script, the user was allowed to specify the range of values for each parameter (WRBW, WRBH, defect depths, etc). The script then entered a nested for loop so that for each combination of user-specified parameters, the createMkmodel.py script was called. Once the geometry-specific input file had been created, the script automatically submitted the job for analysis, waited for the job to complete, and then post processed the output database (ie calculated the stress intensity factor and M<sub>k</sub> factor).

Depending on the availability of computational resources, the submitAll.py script could run approximately 4,000 analyses in 35 hours or about one job every 30 seconds. Thus, the development of automation scripts for this project significantly improved the efficiency of the modelling activities, enabling a large increase in the generation of results against the small amount of time required to write the software.

<sup>1</sup> The flat plate solution was chosen to define the M<sub>k</sub> factor in this report because FEA-based M<sub>k</sub> factor solutions

based on the curved shell geometry stress intensity factor solution in BS 7910 often exhibit non-monotonic behaviour. This causes difficulty when defining a polynomial-based parameterisation of the calculated solutions that is otherwise removed when one chooses the flat plate solution as the normalising term.

## 5 Development of New $M_k$ Factor Solutions

### 5.1 Summary of the results: Type I model

#### 5.1.1 Effect of weld root bead angle

The weld root bead angle was found to have a negligible influence on the stress intensity factor (and hence on the calculated  $M_k$  factor). Before the large parametric study was undertaken, a preliminary sensitivity study was carried out to determine whether the weld root bead angle needed to be included as a parameter. First, for a fixed WRBW and fixed WRBH, the influence of the weld root bead angle on the stress intensity factor is shown in Figure 5. In this figure, the weld root bead angle was varied from 70° to 110° in 10° increments for 10 different defect depths. Each curve in this figure is essentially flat, showing that the stress intensity factors are not significantly affected by the weld angle for fixed values of weld width and height.

Next, the effect of the weld root bead angle as a function of the

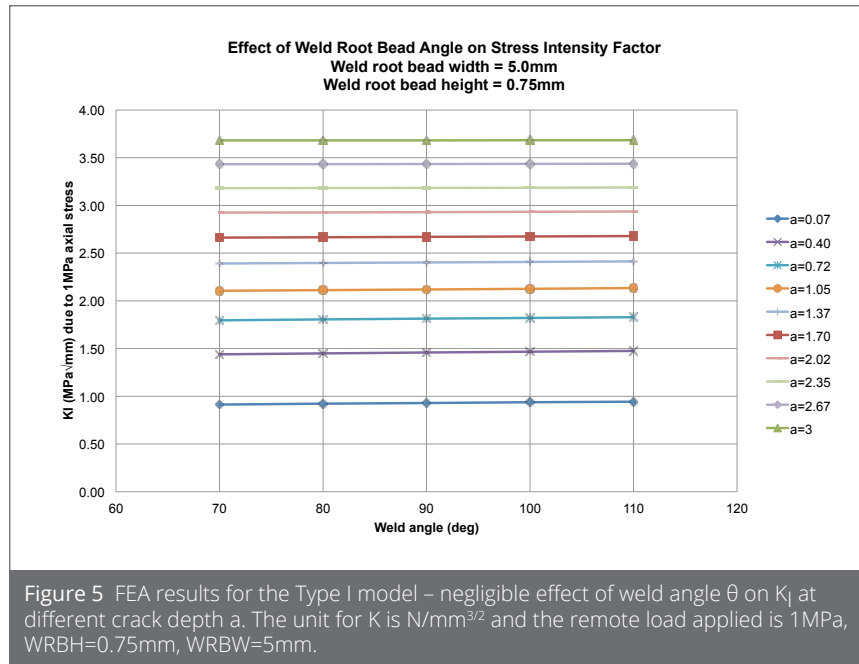


Figure 5 FEA results for the Type I model – negligible effect of weld angle  $\theta$  on  $K_I$  at different crack depth  $a$ . The unit for  $K$  is  $N/mm^{3/2}$  and the remote load applied is 1MPa, WRBH=0.75mm, WRBW=5mm.

WRBH was assessed for two different defect depths: 0.07mm (the smallest considered) and 0.25mm (a defect with  $a/B > 10\%$ ). For each of the two defect depths, the stress intensity factors were computed for a range of WRBHs (with the WRBW fixed at 5.0mm) and for three different weld root bead angles ranging from 70° to 110° degrees which represent the typical weld angles at the girth weld root. For each WRBH, the relative difference between the stress intensity factors calculated at 70° and 90° degrees were computed with respect to the stress intensity factor calculated at 110° degrees (as this angle generated the largest  $K$  value). For both crack

sizes investigated, the difference in  $K_I$  between 90° and 110° degrees increased with increasing WRBH. For the 0.07mm defect, the 90° weld root bead angle only resulted at most in a 2% under-prediction of the stress intensity factor. For the 0.25mm defect, the 90° degree weld root bead angle resulted at most in a 3.3% under-prediction of the stress intensity factor, Figure 6. Thus, although the weld root bead angle does have an influence on the stress intensity factor, it is very small. Consequently, it was determined that it was suitable to assume the weld root bead angle was constant at 90° degree for the remainder of the parametric study.

#### 5.1.2 Effects of WRBW and WRBH

The existing 2D  $M_k$  factor solution in BS 7910:2013 (M.11.1.2) is suitable for cruciform and butt weld geometries and is a function of the flaw depth and normalised attachment length,  $L/B$  (corresponding to  $w/B$  for this study). For attachment lengths with normalised values less than 2 (ie attachments less than two wall thicknesses), the  $M_k$  factor is an explicit function of the normalised attachment length. However, for  $L/B$  in excess of 2, the  $M_k$  factor solution saturates and becomes independent of the attachment length.

The FEA results corresponding to different crack sizes and weld root bead heights are shown in Figure 7 where the weld width is fixed at 5.0mm (so that  $w/B = 0.25$ ). The existing BS 7910  $M_k$  factor solution is also included for comparison. In this figure, the x-axis corresponds to the log-normalised defect depth,  $\log_{10}(a/B)$ . When the WRBH is small ( $h = 0.5$ mm, a typical value at the weld root), the  $M_k$  factor obtained from FEA is significantly lower than the existing BS 7910 solution at small crack sizes. As the height of the weld root bead or the crack size increases, the  $M_k$  factors obtained from the FEA tend to converge monotonically towards the existing 2D BS 7910 solution. There is a small range of defect depths,  $0.02 < a/B < 0.05$ , in which the existing  $M_k$  factor solution is marginally lower for certain weld root bead heights.

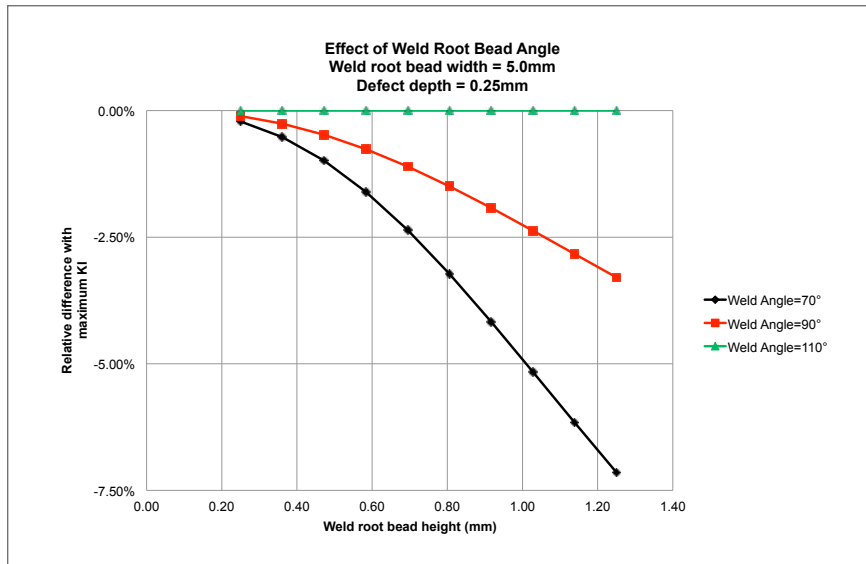


Figure 6 Example showing the effect of weld angle on KI as a function of WRBH for a fixed defect depth,  $a = 0.25\text{mm}$ .  $\theta = 110^\circ$  degrees gave the largest value for each weld root bead height, therefore the curves show the relative difference (% under prediction) compared with this value.

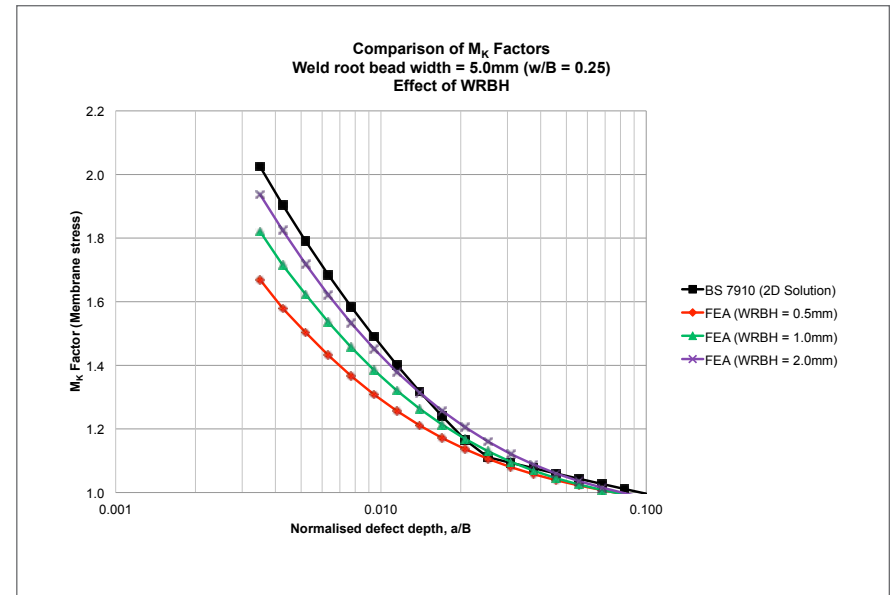


Figure 7 Results of Type I model at a fixed WRBW 5.0mm: dependence of  $M_k$  factor on crack size for various WRBH. The BS 7910 2D  $M_k$  solution with WRBW=5mm is included for comparison.

The results shown in Figure 7 at a fixed crack size provide a consistent picture of the results from the FE parametric study: for fixed values of WRBW, the FEA results produce  $M_k$  factors that are smaller than the existing solution and converge towards the existing solution as the WRBH increases. This demonstrates the benefits of having a new  $M_k$  factor solution that accurately captures the effect of attachment height on  $M_k$ .

An alternative slice of the results is shown in Figure 8. In this figure, for a fixed defect depth (0.23mm), the  $M_k$  factors are shown as a function of the

WRBW for several different values of WRBH. Since the existing 2D  $M_k$  factor solution does not depend on the WRBH, only one curve is shown (black with open square symbols). For very small WRBWs ( $w/B=0.15$ ), the existing and new solutions agree and appear to be independent of the WRBH. However, as the weld width increases, there is an increasing spread between the new FE results and the existing solution. The same trend observed in Figure 7 is reproduced in Figure 8: for each distinct WRBW, the  $M_k$  factor increases with increasing WRBH towards the BS 7910 2D solution. As noted previously, the existing 2D

BS 7910 solution saturates (reaches a constant value) at a normalised weld root bead width of 2.0. This is not shown in Figure 8, but it can be seen that the FE results tend to saturate more quickly, with almost all the curves shown becoming flat by a normalised WRBW of 1.25.

In Figure 9, another slice of the data is shown with the  $M_k$  factors plotted against the normalised WRBH for a fixed defect depth (0.23mm) for various different WRBWs (3.0, 5.0 and 10.0mm). In this figure, the lines corresponding to the BS 7910 solution are flat, because the existing

2D solution does not depend on the attachment height as a variable. The results from the FEA exhibit similar behaviour to that of the dependence of  $M_k$  on the attachment width: the  $M_k$  factor increases with increasing WRBH until it reaches a maximum value. After the maximum value is obtained (typically around  $h/B = 0.125$ ), the  $M_k$  factor reaches a constant value, but tends to decrease slightly from the maximum before saturating.

In Figure 10 a contour plot of the results from the FEA parametric study is shown for the defect depth of 0.23mm ( $a/B = 0.011$ ). The x-axis is

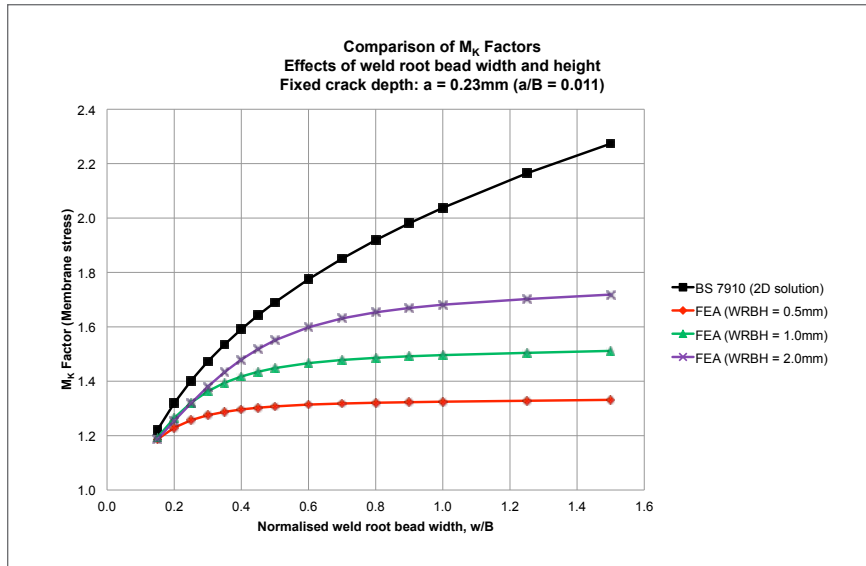


Figure 8 Results of Type I model at a fixed defect depth 0.23mm ( $a/B=0.0115$ ): dependence of  $M_k$  factor on WRBW for various WRBH. The BS 7910 2D  $M_k$  solution is included for comparison.

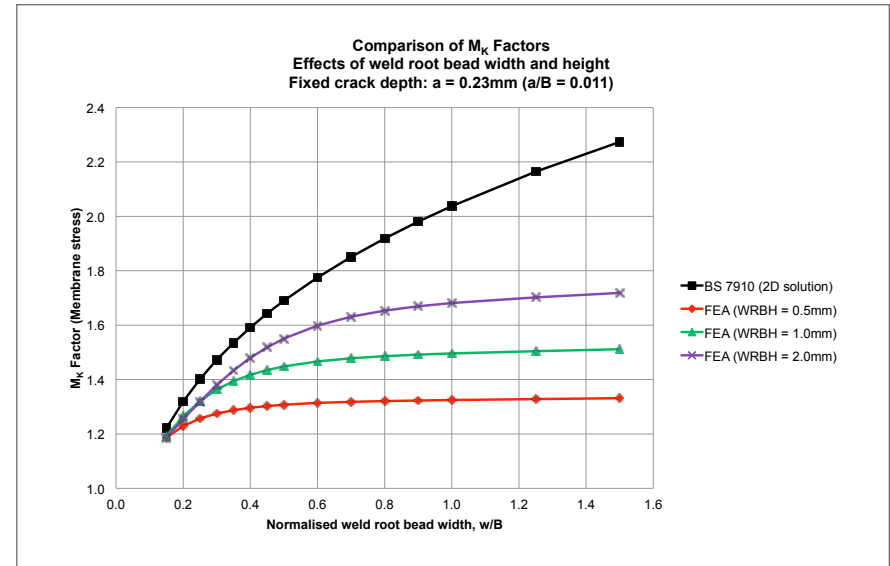


Figure 9 Results of Type I model at a fixed defect depth 0.23mm: dependence of  $M_k$  factor on WRBH for various WRBW. The BS 7910 2D  $M_k$  solution is included for comparison.

the normalised WRBW, and the y-axis is the normalised WRBH. This figure is a single figure representation of the results in Figures 7 and 8, with the colour corresponding to the calculated  $M_k$  factor. In this contour plot, the dependence of the  $M_k$  factor on both the weld width and height is evident. This contour plot is also shown as a surface in Figure 11, with both the colour and the height of the surface representing the magnitude of the  $M_k$  factor. This figure highlights the combined trends for  $w/B$  and  $h/B$ : for combinations of  $w/B > 1.25$  and  $h/B > 0.15$ , which is representative of a typical weld cap, the solution surface becomes flat (red regions). Thus, if the

space of points in the parametric study had included larger weld root bead widths and heights, then a saturation value would have been obtained where the  $M_k$  factor no longer depended on the weld root bead width and height. However, the values for  $w/B$  and  $h/B$  for which the saturation values would occur are beyond those expected for typical pipeline girth weld roots and were not included in the present study.

### 5.1.3 Development of the parametric solutions for Type I model

In light of the summary of the results described above, the initial objective of the research was to

develop a new parametric  $M_k$  factor solution for a Type I model that depended not only on the defect depth and the normalised WRBW, but also on the normalised WRBH.

Based on Figure 7, the non-dimensional variable  $\alpha = \log_{10}(a/B)$  was defined, where  $a$  is the crack depth and  $B$  is the wall thickness (20.0mm). When  $M_k$  is plotted against this non-dimensional parameter, the results appear as shown in Figure 12. In this figure, the form of the BS 7910 2D solution is apparent: when  $M_k$  is plotted against the logarithm of the normalised defect depth (ie the log-normalised defect depth), the

solution appears as two lines with different slopes as derived in the original work by Maddox and Andrews (1990). In contrast, the FEA solution appears as a continuous curve owing to the fact that a significant number of simulations have enabled the behaviour of the  $M_k$  factor solution to be resolved for a large range of defect depths. Polynomial curve fitting revealed that a cubic polynomial provided the optimal fit to the FEA results in that the coefficient of determination, the  $R^2$  score, was exactly 1.0. This means that a cubic polynomial passes through each of the simulation data points exactly.

Table 2 Coefficients for the bivariate polynomial representation of the cubic polynomial coefficients for Type I defects.

Log-normalised weld root bead width index (exponent), j	Log-normalised weld root bead height index (exponent), k	Bivariate surface polynomial coefficients $d_{jk}$ for cubic coefficient $c_1$	Bivariate surface polynomial coefficients $d_{jk}$ for cubic coefficient $c_2$	Bivariate surface polynomial coefficients $d_{jk}$ for cubic coefficient $c_3$	Bivariate surface polynomial coefficients $d_{jk}$ for cubic coefficient $c_4$
0	0	6.2593E-01	-4.8328E-01	-1.3384E+00	-1.5424E+00
0	1	-1.1318E+00	-6.1372E+00	-9.7612E+00	-1.7334E+01
0	2	-2.1673E+00	-1.1235E+01	-1.8304E+01	-3.2446E+01
0	3	-1.9706E+00	-9.7215E+00	-1.6283E+01	-2.9007E+01
0	4	-8.4681E-01	-4.0575E+00	-6.9294E+00	-1.2376E+01
0	5	-1.3906E-01	-6.5522E-01	-1.1316E+00	-2.0201E+00
1	0	-1.2308E+01	-6.1039E+01	-1.0231E+02	-1.7135E+02
1	1	-5.5500E+01	-2.7866E+02	-4.7285E+02	-7.9447E+02
1	2	-9.6500E+01	-4.8814E+02	-8.3877E+02	-1.4121E+03
1	3	-8.0608E+01	-4.1005E+02	-7.1344E+02	-1.2032E+03
1	4	-3.2423E+01	-1.6572E+02	-2.9177E+02	-4.9279E+02
1	5	-5.0435E+00	-2.5888E+01	-4.6079E+01	-7.7922E+01
2	0	-9.7409E+01	-5.0317E+02	-8.3969E+02	-1.3319E+03
2	1	-4.4715E+02	-2.3155E+03	-3.9541E+03	-6.2999E+03
2	2	-7.7885E+02	-4.0496E+03	-7.0676E+03	-1.1304E+04
2	3	-6.4833E+02	-3.3881E+03	-6.0364E+03	-9.6859E+03
2	4	-2.5944E+02	-1.3633E+03	-2.4756E+03	-3.9825E+03
2	5	-4.0131E+01	-2.1206E+02	-3.9180E+02	-6.3148E+02
3	0	-2.7692E+02	-1.5021E+03	-2.3855E+03	-3.5627E+03
3	1	-1.2905E+03	-7.0099E+03	-1.1499E+04	-1.7277E+04
3	2	-2.2756E+03	-1.2402E+04	-2.0985E+04	-3.1701E+04
3	3	-1.9121E+03	-1.0473E+04	-1.8248E+04	-2.7696E+04
3	4	-7.7050E+02	-4.2452E+03	-7.5971E+03	-1.1574E+04
3	5	-1.1979E+02	-6.6423E+02	-1.2175E+03	-1.8601E+03
4	0	-3.1825E+02	-1.7883E+03	-2.5813E+03	-3.5832E+03
4	1	-1.5070E+03	-8.4851E+03	-1.2838E+04	-1.8028E+04
4	2	-2.6968E+03	-1.5245E+04	-2.4098E+04	-3.4167E+04
4	3	-2.2962E+03	-1.3058E+04	-2.1495E+04	-3.0732E+04
4	4	-9.3588E+02	-5.3600E+03	-9.1487E+03	-1.3169E+04
4	5	-1.4691E+02	-8.4781E+02	-1.4939E+03	-2.1616E+03
5	0	-1.2462E+02	-7.1635E+02	-8.7543E+02	-1.0754E+03
5	1	-6.0068E+02	-3.4634E+03	-4.5684E+03	-5.7833E+03
5	2	-1.0928E+03	-6.3336E+03	-8.9328E+03	-1.1571E+04
5	3	-9.4492E+02	-5.5170E+03	-8.2594E+03	-1.0903E+04
5	4	-3.9048E+02	-2.2994E+03	-3.6245E+03	-4.8561E+03
5	5	-6.2033E+01	-3.6863E+02	-6.0709E+02	-8.2259E+02

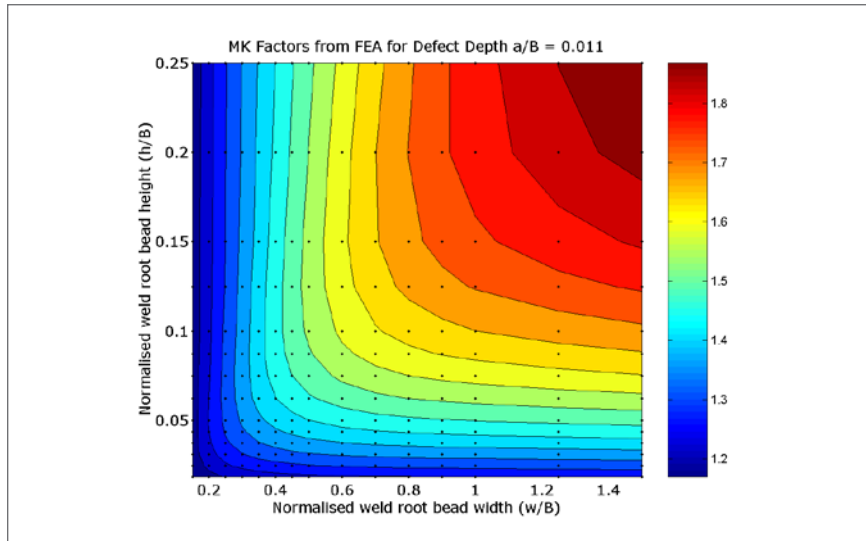


Figure 10 Contour plot of the calculated  $M_k$  factors for a defect depth of 0.23mm ( $a/B = 0.011$ ), Type I model. The dependence of the  $M_k$  factor on the WRBW and the WRBH is evident.

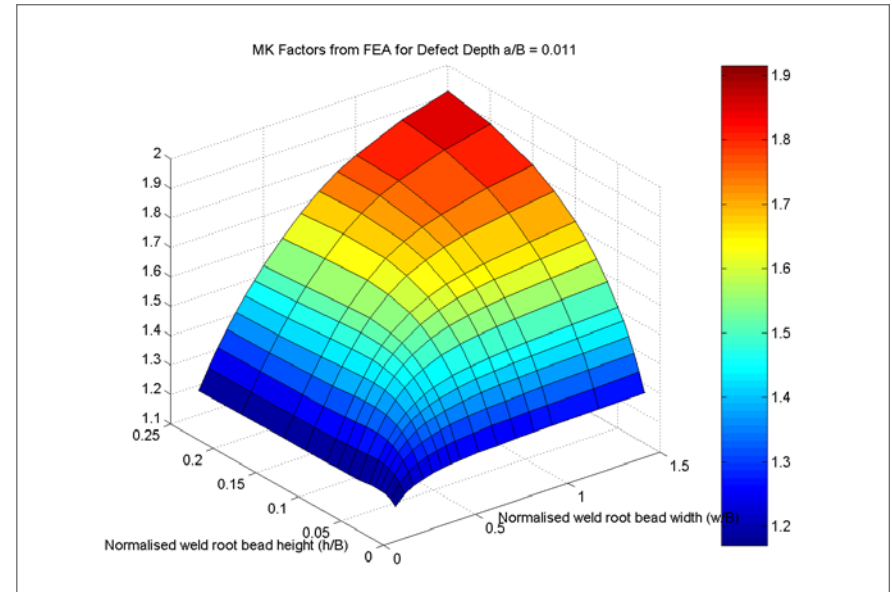


Figure 11 Surface image of the contour plot shown in Figure 10, Type I model.

Therefore, it was determined that the best representation of the  $M_k$  factors was an equation of the form:

$$5 \quad M_k(\alpha, w, h) = c_1 \alpha^3 + c_2 \alpha^2 + c_3 \alpha + c_4$$

For each combination of  $w$  and  $h$  analysed during the parametric FEA study, the cubic polynomial coefficients,  $c_1$  to  $c_4$ , appearing in Equation [5] were determined using least squares regression.

The next step in the development of the new parametric  $M_k$  factor solution was to determine a way of mapping an arbitrary pair of WRBW and WRBH values to a set of cubic polynomial coefficients. It is useful to

observe the shape of the coefficient surfaces defined by plotting  $c_i$  as a function of  $w/B$  and  $h/B$ . An example of such a surface is shown in Figure 13 for the cubic coefficient  $c_1$  where it can be seen that the surface depends smoothly on the in-plane parameters  $w/B$  and  $h/B$ . However, the surface exhibits rapid changes in both coordinates with multiple local maxima, minima and inflection points. As a consequence, a high-order multivariate polynomial was required to accurately represent the surface. The surface was represented in the form:

$$6 \quad c_i(\bar{w}, \bar{h}) = \ln \left\{ \sum_{j=1}^5 \sum_{k=1}^5 \sigma_{jk} [\log_{10}(\bar{w})]^j [\log_{10}(\bar{h})]^k \right\}$$

In Equation [6], the variables  $w$  and  $h$  are log-normalised using a logarithm base 10, and a natural logarithm (log base  $e$ ) is taken of the entire polynomial sum. For each cubic polynomial coefficient  $c_i$  ( $i = 1, 2, 3, 4$ ), least squares regression was used to determine the optimal  $d_{jk}$  coefficients with the resulting coefficients shown in Table 2.

#### 5.1.4 Verification of the new parametric $M_k$ factor solutions

The parametric solutions have been verified against all of the simulation data. For each pair of  $w$  and  $h$  values, the simulation data for each defect depth were compared with the predicted  $M_k$  factor values for the

same defect depths obtained by using the values in Table 2 and Equations [5] and [6]. To measure how well the simulation results were replicated by the parametric model, both the  $R^2$  score and the root mean square errors were calculated. The results indicate that the cubic equation fit with the coefficients in Table 2 provides very accurate results:

- For all pairs of  $w$  and  $h$  that were analysed, the minimum  $R^2$  score was 0.992 and the mean  $R^2$  score was 0.997;
- The maximum root mean square error was 2% and the mean root mean square error was 0.03%.

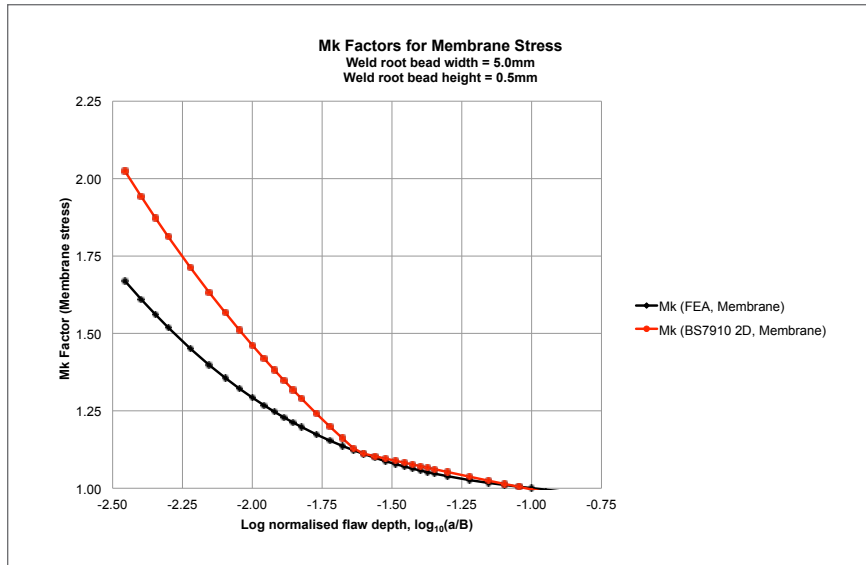


Figure 12  $M_k$  factor curves shown in Figure 7, but plotted against the logarithm (base 10) of the normalised defect depth (WRBW=5.0mm, WRBH=0.5mm), Type I model.

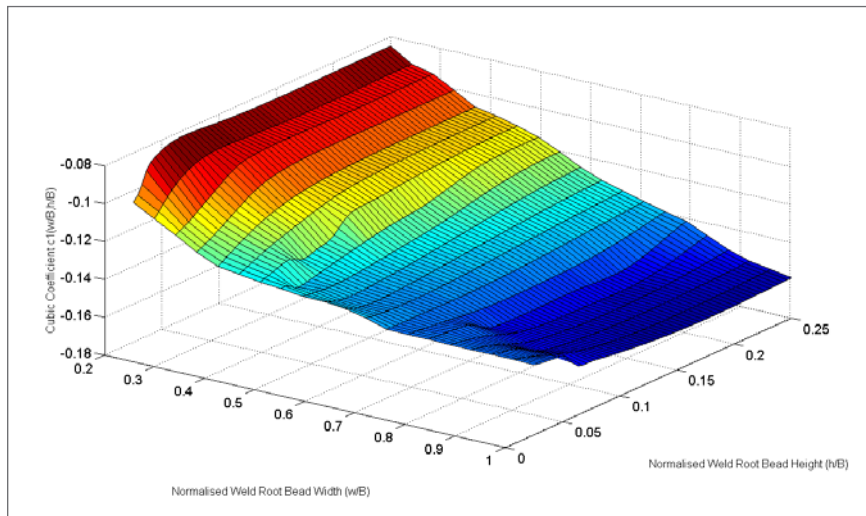


Figure 13 Surface defined by plotting the cubic coefficient  $c_1$  as a function of the normalised weld root bead width ( $w/B$ ) and the normalised weld root bead height ( $h/B$ ).

Table 3 Coefficients for the quadratic equation for each of the four cubic coefficients ( $c_i$ ) for Type II defects.

	$c_1$	$c_2$	$c_3$	$c_4$
$d_{i,1}$	9.9395E-01	-4.0688E+00	-4.1917E+00	-1.4097E+00
$d_{i,2}$	-6.4612E-01	1.0132E+00	-7.0390E-02	1.2472E-01
$d_{i,3}$	-1.4010E-01	-4.9899E-01	-7.0482E-01	6.3773E-01

The regression was further verified by choosing random width and height values that were not analysed in the FE parametric study and therefore not used to generate the parametric solution.

For example, consider the WRBW value  $w = 7.63\text{mm}$  and the WRBH value  $h = 1.21\text{mm}$ . The FE automation code was re-run to determine the  $M_k$  factors for Type I defect depths ranging from 0.07 to 3.00mm for these specific values of  $w$  and  $h$ . The newly calculated values from FEA were compared with the predictions from the new parametric solution and the results are very good. Considering all of the defect heights analysed, the:

- Maximum relative error from the parametric equations is 0.29%;
- Average relative error from the parametric equations is 0.12%.

Thus, the proposed new parametric  $M_k$  factor solutions can be considered valid for Type I models over the domain range considered:

- Wall thickness to outer diameter ( $B/D$ ) equal to 0.049;
- Normalised WRBWs,  $w/B$ , between 0.15 and 1.0;
- Normalised WRBHs,  $h/B$ , between 0.0125 and 0.25;
- Normalised defect depths,  $a/B$ , between 0.0035 and 0.15.

### 5.1.5 Applying the new parametric $M_k$ factor solutions

For a given value of WRBW,  $w$ , and WRBH,  $h$ , the cubic polynomial coefficients in Equation [5] need to be determined. For each  $c_i$  this is done as follows:

- For each  $i = 1$  to 4, the appropriate column of  $d_{jk}$  values from Table 2 are substituted into Equation [6];
- Once these coefficients are specified, the log-normalised values of  $w$  and  $h$  are inserted into the equation, and the  $c_i$  value is calculated;
- Once each of the  $c_i$  coefficients is known, Equation [5] can be used in conjunction with the log-normalised defect depth to calculate the  $M_k$  factor.

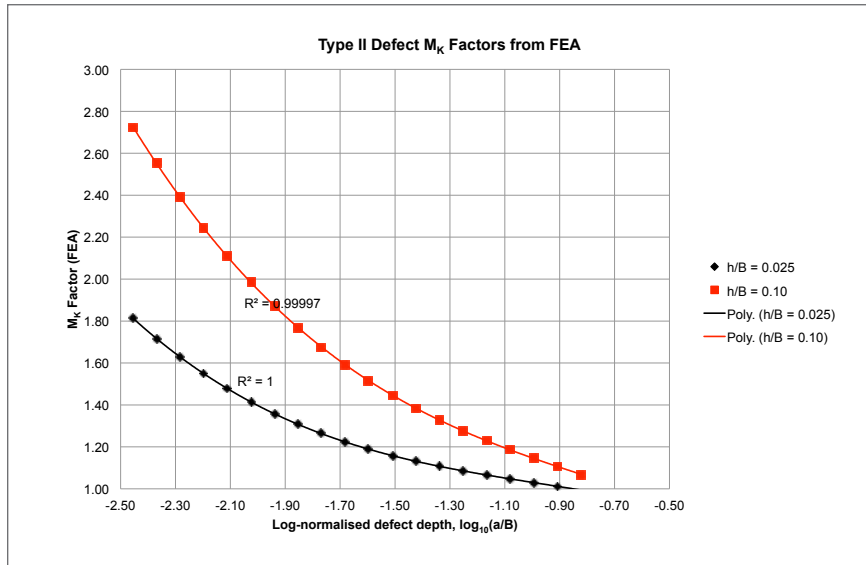


Figure 14 Polynomial regression showing the optimal fit of a cubic polynomial to two Type II defect  $M_k$  factor curves when plotted against the log-normalised defect depth, WRBW=5.0mm.

A Microsoft Excel spreadsheet has been set up to allow for easy implementation and use of the methods described above. It is envisaged that, subject to further verification and validation, the new  $M_k$  factor solutions will be incorporated in CrackWISE®. This further exercise would include the effect of ratio of wall thickness to diameter (B/D) on the  $M_k$  factor solution. However, this is not likely to require an extensive parametric study, because it is anticipated that the effect of B/D will be to shift the weld root bead profile stress concentration factor by a factor proportional to  $e^{-\sqrt{B/D}}$  (Lotsberg, 2008).

## 5.2 Summary of results: Type II model

### 5.2.1 Development of the parametric solutions

The procedure that was applied for Type I models was applied for Type II, except that in the latter model, the WRBW is not an explicit parameter. As described previously, Type II defects are the limiting case of Type I defects as the weld root bead width increases to become very large; in other words, if the Type I defect parametric study had included much larger values of weld root bead width, then the Type II solutions would be the saturation values for Type

I defects with large  $w/B$  values. The calculated  $M_k$  factors for two Type II defects (one with  $h/B = 0.025$  and one with  $h/B = 0.1$ ) are shown in Figure 14. As before, it can be seen that a cubic polynomial provides the optimal fit with an  $R^2$  score of 1.0, and therefore, the formulation of the  $M_k$  factor equation is still the same as the Type I equation, except that the dependence on weld root bead width is removed:

$$7 \quad M_k(\alpha, h) = c_1 \alpha^3 + c_2 \alpha^2 + c_3 \alpha + c_4$$

The cubic coefficients now depend only on the WRBH, and therefore a quadratic equation (as opposed to a quadratic surface for Type I defects) was sought in the following form:

$$8 \quad c_i(h/B) = d_{i,1}(h/B)^2 + d_{i,2}(h/B) + d_{i,3}$$

A least squares regression, similar to that detailed for Type I defects, was undertaken and the resulting coefficients are shown in Table 3.

### 5.2.2 Verification of the new parametric $M_k$ factor solutions

The accuracy of the new parametric  $M_k$  factor solution for Type II defects has been verified in two ways.

Firstly, in Figure 15, the result of representing the cubic polynomial coefficients from Equation [7] by the quadratic form in Equation [8] is shown. In this figure, for each  $h/B$  value, the solid symbols represent

the values of  $c_1$  to  $c_4$  obtained by representing the  $M_k$  factor solution by the cubic polynomial in Equation [7]. The dashed lines show the best-fit quadratic equation using the  $d_i$  coefficients shown in Table 3. It is clear that, except for some very small variation in the cubic coefficients at low  $h/B$  values, the quadratic equation provides a very good approximation to the calculated  $c_i$  values.

Secondly, the accuracy of combining Equations [7] and [8] to represent Type II defect  $M_k$  factors was assessed. In Figure 16, for four different normalised weld root bead height values, the  $M_k$  factor solutions are shown. In this figure, the open symbols connected by solid lines correspond to the solutions calculated from the FE models; the solid symbols connected by dashed lines correspond to the solutions calculated using Equations [7] and [8]. The agreement between the two curves is very good and is representative of the accuracy of the parametric solution for all other values of normalised WRBH not shown in the figure. Specifically, the largest absolute relative error of the approximations shown is 2.3%, corresponding to a very small normalised defect depth for the  $h/B = 0.05$  curve. The average relative error is less than 1% for all of the curves shown.

### 5.2.3 Applying the new parametric $M_k$ factor solutions

For a given value of WRBH,  $h$ , the cubic polynomial coefficients in Equation [7] need to be determined.

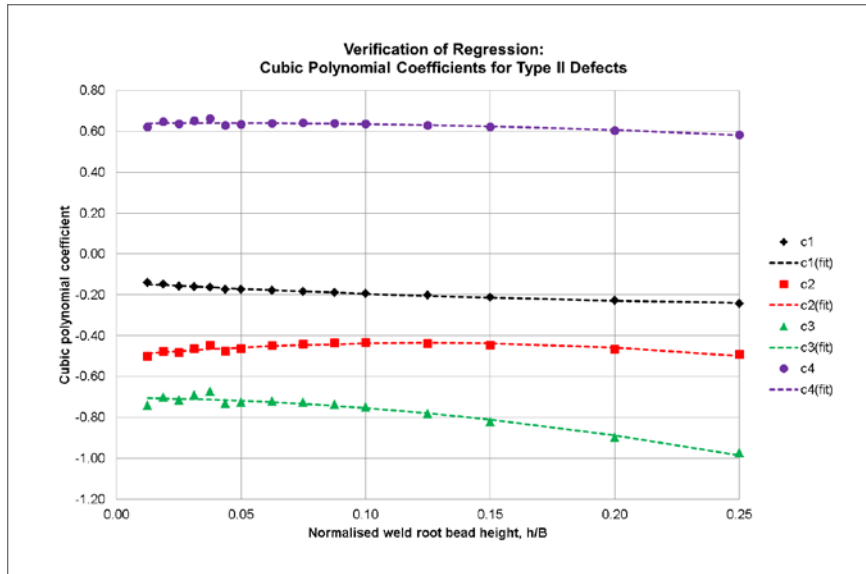


Figure 15 Verification of the cubic polynomial fit used for the Type II  $M_k$  factor solution.

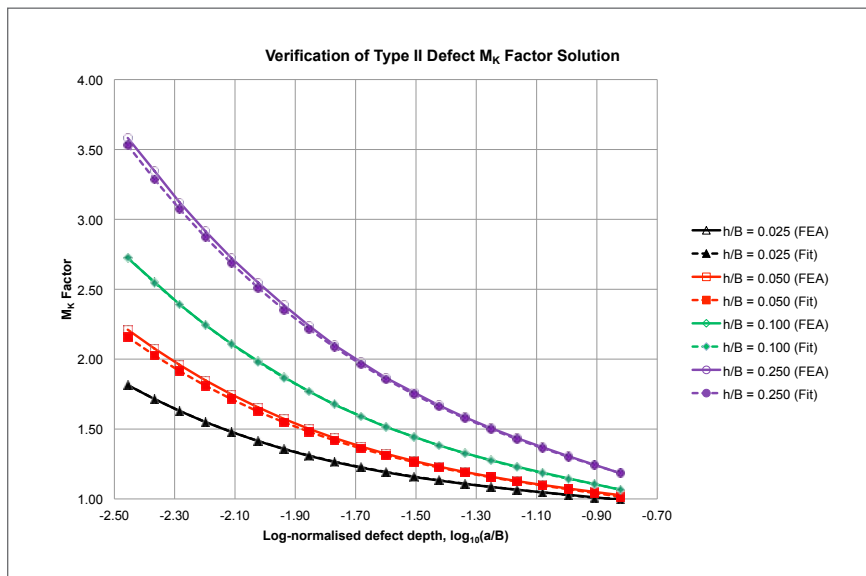


Figure 16 Verification of the parametric representation of the Type II  $M_k$  factor solution.

For each  $c_i$  this is done as follows:

- For each  $i = 1$  to 4, the appropriate column of  $d_{ij}$  values from Table 3 are substituted into Equation [8] along with the normalised WRBH to determine  $c_1$  to  $c_4$ ;
- Once these coefficients have been determined, the log-normalised defect depth is inserted into Equation [7] with the  $c_i$  values to calculate the  $M_k$  factor.

### 5.3 Considerations for Type III model

Having developed solutions for both Type I and II defects through least squares regression and detailed parametric studies, Type III defects were then considered. A series of Type III models was developed and the resulting  $M_k$  factor solutions were analysed.

For a model with defect depth  $a$ , weld root bead height  $h$ , and weld root bead width  $w$ , the following variables are defined:

- Let  $\lambda$  be a variable representing the hi-lo,  $0 \leq \lambda \leq h$ ;
- Let  $M_k^I(a, h, w)$  be the Type I  $M_k$  factor for the variables  $a$ ,  $w$  and  $h$ ;
- Let  $M_k^{II}(a, h)$  be the Type II  $M_k$  factor for the variables  $a$  and  $h$ .

The following observation was made:

$$9 \quad M_k^{III}(a, w, h, \lambda) = \left(1 - \frac{\lambda}{h}\right) M_k^I(a, w, h) + \left(\frac{\lambda}{h}\right) M_k^{II}(a, h)$$

Specifically, Equation [9] indicates that a Type III defect is the convex combination of Type I and Type II defects with the coefficients in the convex combination determined by the ratio of the hi-lo to the WRBH.

Verification of Equation [9] is shown in two figures. In Figure 17, simulations for a series of defects with WRBH equal to 1.0mm and WRBW 5.0mm were carried out. Three sets of simulations were performed: one each for Type I, II and III (hi-lo equal to 0.5mm) defects. The resulting  $M_k$  factors were calculated and are shown as solid curves in Figure 17. Additionally, the convex combination of the Type I and II defects is shown as a green dashed curve. The convex combination replicates the simulation results to within 1-2% accuracy. The same exercise was repeated but with the Type III defects having hi-lo equal to 0.25mm. The results are shown in Figure 18. Again, the convex combination equation replicates the simulation results to a high level of accuracy.

Therefore, having developed detailed parametric equations for Types I and II defects, it has been demonstrated that the  $M_k$  factors associated with Type III defects can be produced by using a convex combination of the corresponding Types I and II defect solutions.

Table 4 Comparison of crack sizes between experiment and prediction.

Block No.	Measurements, mm		FM prediction, mm		Difference in crack depth between measurement and prediction, %
	Crack depth a	Crack length 2c*	Crack depth a	Crack length 2c	
0 (initial)	1.6	13.5	1.6	13.5	0.0
1	2.1	-	2.2	14.2	3.3
2	3.0	-	3.2	16.4	5.9
3	4.6	-	5.1	22.2	10.7

\*: Difficult to determine the crack lengths from the fracture surface for some blocks.

## 6 Assessment of Accuracy of the $M_k$ Solution Derived

### 6.1 Introduction

In a Joint Industry Project (JIP) undertaken by TWI, fatigue performance of full-scale girth welded pipes was investigated under both constant amplitude (CA) and variable amplitude (VA) loading (Zhang and Maddox, 2011 and 2014). Comprehensive post-test examinations were carried out for all full-scale girth welds tested, including measurements of wall thickness, weld root hi-lo, and WRBH at each gauge location. Therefore, the opportunity was taken to use the results from that JIP to assess the accuracy of the FE  $M_k$  solutions developed in this project, in terms of both fatigue crack growth and S-N curve approaches.

The pipes used in the JIP had an outside diameter of 406mm and a wall thickness of 19.1mm and were

made of seamless steel pipe to API 5L-X70 specification. The girth welds were made from the outside in the 5G position by pulsed gas metal arc welding/gas metal arc welding (PGMAW/GMAW) onto copper backing. The weld cap at each start/stop position was ground flush with the pipe surface. Most of the pipes contained two girth welds. All welds were shown to be acceptable to a typical steel catenary riser (SCR) specification. Full-scale girth welded pipes were fatigue tested in resonance rigs. An axial tensile mean stress of 150MPa was applied by pressurising the pipes internally with tap water. All the tests were conducted in air at ambient temperature and loading frequencies 25-30Hz. A total of thirty-three welds had been fatigue tested, eleven under CA loading and twenty two under VA loading. Details of the full-scale fatigue test under VA loading have been reported (Zhang and Maddox, 2011 and 2014). In summary, the spectra were divided into six sub-blocks and,

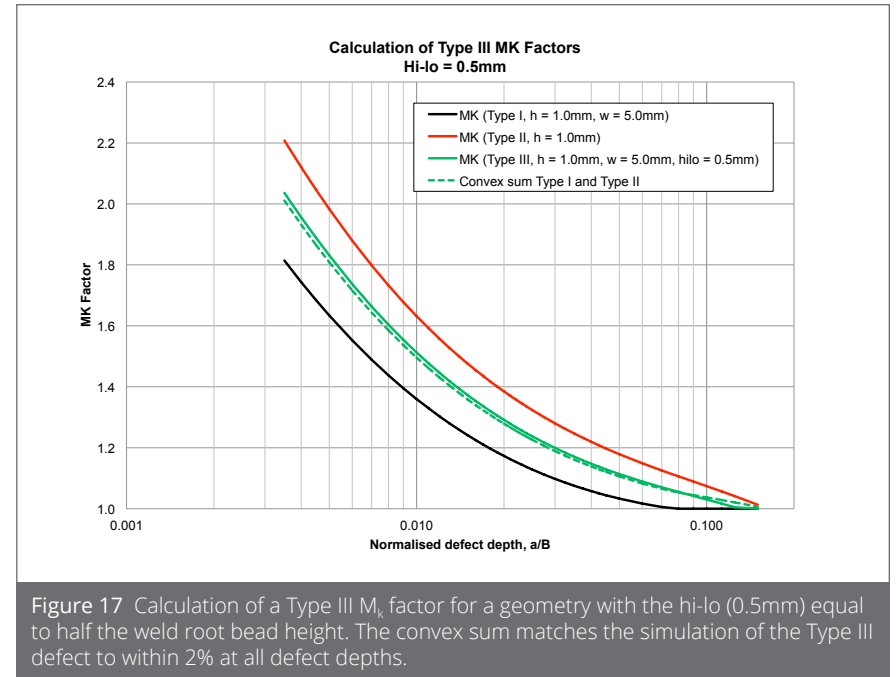


Figure 17 Calculation of a Type III  $M_k$  factor for a geometry with the hi-lo (0.5mm) equal to half the weld root bead height. The convex sum matches the simulation of the Type III defect to within 2% at all defect depths.

in each sub-block, the stress range increased from the minimum value to a peak value and then decreased to the minimum value. An example spectrum is shown in Figure 19 where the minimum stress range was 60MPa and a total of three loading blocks (repeats) are shown. Although the maximum stress range was the same for all spectra, the minimum stress ranges varied, from 80 to 40MPa in order to investigate the effect of low stresses on fatigue performance of the girth welds in a loading spectrum.

Almost all cracking was found to occur at the weld root toes. The failure locations were often characterised by relatively poor weld root bead profiles,

with the average WRBH at the worst location along the circumference of the girth welds being ~0.5mm.

### 6.2 Estimating fatigue crack growth

For those specimens tested under VA loading, beach marks were produced on the fracture surfaces. They provide a good opportunity to assess the accuracy of the  $M_k$  solution developed in this project by comparing the crack growth measured on the fracture surfaces with those calculated using the fracture mechanics-based approach, based on integration of the fatigue crack growth law as detailed in BS 7910. Within each block, there were six beach marks,

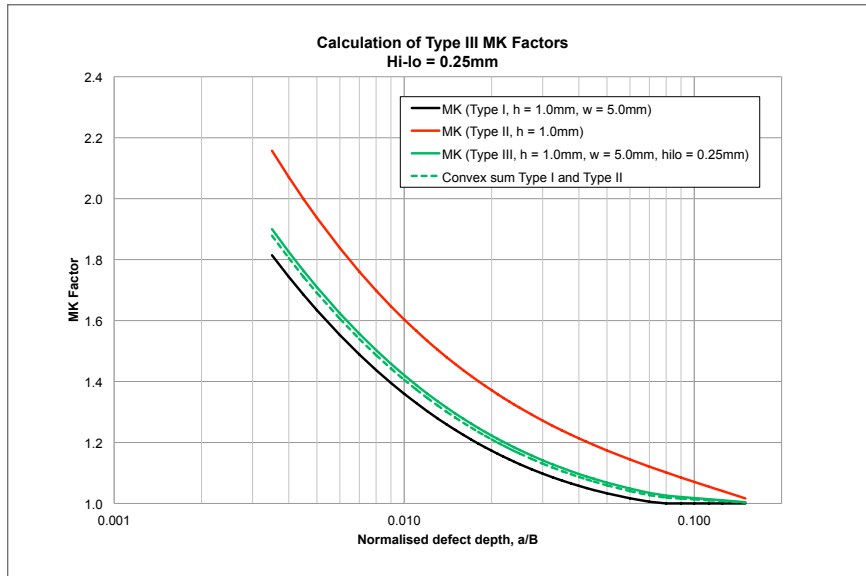


Figure 18 Calculation of a Type III  $M_k$  factor for a geometry with the hi-lo (0.25mm) equal to 25% the weld root bead height. The convex sum matches the simulation of the Type III defect to within 2% at all defect depths.

each corresponding to the peak stress in the loading spectrum. As  $M_k$  has a strong effect on fatigue crack growth only near the surface, beach marks corresponding to short fatigue cracks are required to examine the accuracy of the  $M_k$  solution. Although beach marks were seen on the fracture surfaces of many specimens, beach marks from relatively short cracks were obtained from only one specimen as shown in Figure 20. The pipe (No.17) was tested under a spectrum with a minimum stress range of 50MPa and a block length of 603,330 cycles. The weld failed after 31.3 blocks (ie at 18,884,229 cycles). The first visible beach mark corresponded to a

crack depth of 1.6mm and length of 13.5mm. After three blocks of the VA loading spectrum, the crack had grown to a depth of 4.65mm. The weld root bead of this girth weld corresponded to the Type II defect model, with the WRBH=hi-lo=0.85mm and w=3mm.

Fatigue crack growth rate,  $da/dN$ , can be expressed by the following Paris power law equation:

$$10 \quad \frac{da}{dN} = C(\Delta K)^m$$

Where C and m are material constants and  $\Delta K$  is the stress intensity factor range. The mean crack growth law given in BS 7910

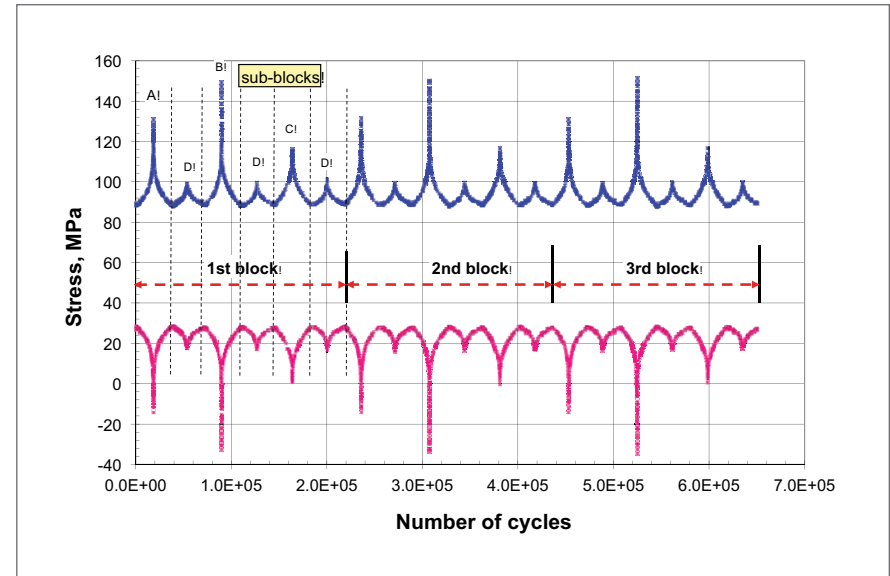


Figure 19 Cyclic loading sequence (peak stresses in each loading and unloading cycle) that illustrates the loading block in the VA testing (Zhang and Maddox, 2014). The minimum stress range was 60MPa in this example.

for steels in air with stress ratio  $R \geq 0.5$  was used. This is in two stages with  $m = 5.10$  and  $C = 4.8 \times 10^{-18}$  initially and then  $m = 2.88$  with  $C = 5.86 \times 10^{-13}$  after  $\Delta K = 196 \text{ N/mm}^{3/2}$ .

For the semi-elliptical crack, crack growth was calculated in both the a- (depth) and c- (surface) directions. For such calculations using the 2D  $M_k$  solution developed in this project, the solution is applied directly for calculating  $\Delta K$  at the deepest point in the crack. Thus,  $M_{ka}$  decreases as 'a' increases. However, in the absence of a solution for  $M_{kc}$ , at the ends of the crack, a constant value is assumed for assessing crack growth in the c direction. As suggested in BS 7910

(2013), the  $M_k$  value at a crack depth of 0.15mm was used for the intersection of surface flaws with the weld toe, ie,  $M_{kc}$  is equal to  $M_{ka}$  at 0.15mm. This is a conservative approach (Maddox, 1997).

Table 4 and Figure 21 compare the prediction and the experimental data for the fatigue crack extensions with an increasing number of blocks. It can be seen that the prediction agreed well with the experimental data, suggesting that the  $M_k$  solution developed in this project was appropriate for characterising the effect of the weld root bead profile on fatigue crack growth rate (FCGR) in this case.

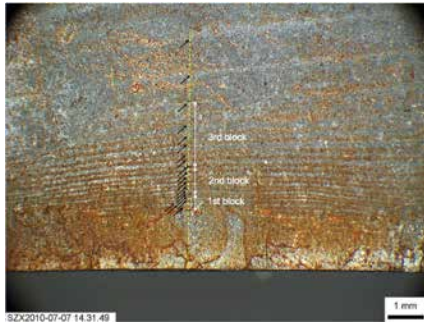


Figure 20 Fracture surface of the W1 weld in pipe S17. The beach marks corresponding to each peak load are marked with arrows. Each block is composed of six beach marks (stress peaks). The a/B ranged from 0.08 to 0.24 in the three blocks.

Although more analyses from fatigue crack growth beach marks would be desirable to assess the accuracy of the  $M_k$  solution developed, it was difficult to obtain beach marks from short fatigue cracks (<1mm). As a result, further assessments using an S-N curve approach have been undertaken as described below.

### 6.3 Estimating the constant amplitude S-N curve

Six pipes, with a total of eleven girth welds, were tested to establish the CA S-N curve. The test results are plotted in Figure 22 in terms of nominal stress range. Assuming that all the results from failed welds lie on the same S-N curve, regression analysis produced the mean S-N curve  $\Delta S^{3.47} N = 4.53 \times 10^{13}$ , with a standard deviation (SD) of log(N) of 0.148. On the basis

Table 5 Comparison of the predicted fatigue lives between the DNV F101:2013 guidance and the  $M_k$  solution developed in the present project.

Case No.	Type of model	Stress range, MPa	WRBH, mm	Hi-lo, mm	Pred. fatigue life, cycles		Difference, %
					DNV-2013	Present $M_k$	
1	I	120	1.0	0.0	$4.35 \times 10^6$	$4.57 \times 10^6$	4.8
2	I	120	0.25	0.0	$4.35 \times 10^6$	$5.61 \times 10^6$	22.5
3	II	120	1.0	1.0	$3.01 \times 10^6$	$1.56 \times 10^6$	-93.0
3-a	II	200	1.0	1.0	$3.89 \times 10^5$	$2.71 \times 10^5$	-43.5
4	II	120	0.5	0.5	$3.60 \times 10^6$	$2.65 \times 10^6$	-36.0
5	II	120	0.25	0.25	$3.95 \times 10^6$	$3.72 \times 10^6$	-6.2
6	III	120	1.0	0.25	$3.95 \times 10^6$	$3.30 \times 10^6$	-19.7
7	III	120	1.0	0.5	$3.60 \times 10^6$	$2.50 \times 10^6$	-44.0
8	III	120	1.0	0.75	$3.29 \times 10^6$	$1.95 \times 10^6$	-68.7
8-a	III	200	1.0	0.75	$4.11 \times 10^5$	$3.10 \times 10^5$	-32.6

Notes: The initial flaw size was assumed to be 0.07 by 1mm, the 2-stage mean FCGR curve given in BS 7910 for steels in air with  $R \geq 0.5$  was used. The weld root bead width, w, was 3mm.

that some failures were obtained at endurance beyond  $10^7$  cycles including one at  $4.4 \times 10^7$  cycles, a two-stage S-N curve was proposed, with a slope transition at  $5 \times 10^7$  (Zhang and Maddox, 2014; BS 7608, 2014). By assuming a slope of m+2 for the curve after  $5 \times 10^7$  cycles, the parameter A for the curve after  $5 \times 10^7$  cycles was determined to be  $1.22 \times 10^{17}$ . The two-stage mean, lower and upper bound (mean-2SD and mean+2SD) S-N curves are shown in Figure 22.

Welds inevitably contain flaws, notably the sharp non-metallic intrusions at the weld toes from which fatigue cracks have been observed to propagate (Signes et al, 1967). In that work, close examination of fillet welds

in steel identified weld toe flaw sizes ranging from 0.15 to 0.4mm. Based on post-test examination of macro-sections of the girth welds tested in the JIP, the quality was generally better than that found by Signes et al, with weld toe flaw depths of ~0.07mm on average. Two examples of the weld root toe flaws are shown in Figure 23, with that in Figure 23a showing initiation of a fatigue crack at the weld root bead toe.

Therefore, in the following fracture mechanics analyses, the initial flaw size was assumed to be 0.07mm. The initial flaw was assumed to have a semi-elliptical shape and a shallow crack aspect ratio, with  $a/c=0.14$  ( $2c=1\text{mm}$ ). Again the  $M_{kc}$  was assumed

to be constant and equal to the  $M_k$  in depth direction ( $M_{ka}$ ) at  $a=0.15\text{mm}$ . The weld root was assumed to have the Type II profile. A WRBH of 0.5mm, which represents the average size at the worst location along the circumference of all the girth welds, was assumed in the calculations. In addition, two more predictions were made by adopting the lower and upper bound values for the WRBH: 0.25 and 0.75mm. The predicted S-N curves are shown in Figure 22 for comparison with the experimental mean, lower and upper bound S-N curves. The predicted mean S-N curve agreed well with the experimental mean S-N curve at fatigue lives  $\leq 5 \times 10^6$  cycles. At fatigue lives greater than  $5 \times 10^6$  cycles, the predicted lives were greater. This

is not surprising since there were few failures in the long life regime and the data exhibited large scatter. Despite the failure at  $4.4 \times 10^7$  cycles, several welds were unfailed at fatigue lives far beyond the mean S-N curve.

It can also be seen that the scatter between the lower and upper bound S-N curves for WRBH 0.25 and 0.75mm is much smaller than the experimental scatter. This suggests that, except for the WRBH, other parameters could also contribute to the experimental data scatter, for example, variations in initial flaw size, residual stresses, misalignment, etc. It should also be noted that crack initiation life was not considered in the analysis. For a blunt flaw like that in Figure 23b, fatigue crack initiation life could play an important part in the total fatigue life, especially in the long life regime.

## 7 Examination of the Guidance in Standards

As described in the introduction, DNV GL F101 provides guidance on ECA of flaws at the girth weld root toe. The most recent version (DNV, 2013) requires an input of the WRBW and an inclusion of the misalignment-induced SCF. BS 7910 does not provide specific guidance on ECA of girth weld roots. The 2D solution requires an input for only the weld width  $w$ . It is understood that, when assessing weld root, the appropriate  $w$  should represent the WRBW. Therefore, the method is the same as that given in the DNV F101, 2013. Therefore, an opportunity was

**Table 6** Comparison of the predicted fatigue lives between the DNV F101:2013 guidance and the  $M_k$  solution developed in the present project by increasing the WRBW (refer to Table 5 regarding the Case No.).

Case No.	Type of model	Stress range, MPa	WRBW, mm	WRBH, mm	Hi-lo, mm	Pred. fatigue life, cycles		Difference, %
						DNV-2013	Present $M_k$	
3	II	120	5	1.0	1.0	$1.83 \times 10^6$	$1.56 \times 10^6$	-17
3-b	II	120	6	1.0	1.0	$1.52 \times 10^6$	$1.56 \times 10^6$	3
4	II	120	5	0.5	0.5	$2.16 \times 10^6$	$2.65 \times 10^6$	18
5	II	120	5	0.25	0.25	$2.35 \times 10^6$	$3.72 \times 10^6$	37
6	III	120	5	1.0	0.25	$2.35 \times 10^6$	$3.30 \times 10^6$	29
7	III	120	5	1.0	0.5	$2.16 \times 10^6$	$2.50 \times 10^6$	14
8	III	120	5	1.0	0.75	$1.99 \times 10^6$	$1.95 \times 10^6$	2

taken to examine the guidance by comparing the predicted fatigue lives, based on the approaches suggested in the standards, with both the experimental data and the predicted lives based on the  $M_k$  solution developed in the present project.

In all fatigue crack growth life calculations, the input parameters were the same as those used in Section 6.3, ie, an initial surface-breaking flaw 0.07mm deep and 1.0mm long, the two-stage mean FCGR law from BS 7910, WRBW=3mm, WRBH=0.5mm, and weld root profile corresponding to the Type II defect model. Figure 24 shows four S-N curves for comparison:

- The experimental mean S-N curve determined from the JIP (the mean curve shown in Figure 22 up to  $10^7$  cycles);
- The S-N curve predicted by using the FE  $M_k$  solution developed in

the present project. As described before, the predicted S-N curve agreed well with the experimental one;

- The S-N curve predicted in accordance with the guidance given in DNV F101:2012, ie,  $w$  = weld cap width (13mm in the present case) and excluding misalignment-induced SCF. It can be seen that it significantly under-estimated the actual fatigue life, by about 60%. This was because WRBW has a strong effect on  $M_k$  solution;
- The S-N curve predicted in accordance with the DNV F101:2013, ie,  $w$ =weld root bead width (3mm in the present case) and inclusion of the misalignment-induced SCF (calculated assuming hi-lo=0.5mm so the centre-line offset is 0.25mm). The predicted S-N curve agreed well with the experimental one, but over-estimated the fatigue life in the long life regime ( $>10^6$  cycles). The

predicted life was also longer than that calculated based on the present  $M_k$  solution.

The above results suggest that, if there is a hi-lo at the weld root (Types II and III defect models) and the WRBW is relatively small, use of the guidance given in DNV F101:2013 could underestimate the actual  $M_k$  effect as can be seen in Figure 25. In this figure, all DNV F101:2013  $M_k$  curves were based on the BS 7910 2D  $M_k$  multiplied by the misalignment induced SCF to allow for a direct comparison with the present FE  $M_k$  solutions which already include the SCF in the model. It will be seen from Figure 25 that, when the WRBW is relatively small, at 3mm, DNV F101:2013 underestimates the  $M_k$ , as developed in this work, for most crack sizes of interest, especially at the higher hi-lo (1mm). WRBW has a strong effect on the BS 7910 2D  $M_k$  solution. When  $w$  was increased to 5mm in the BS 7910 2D  $M_k$  solution,

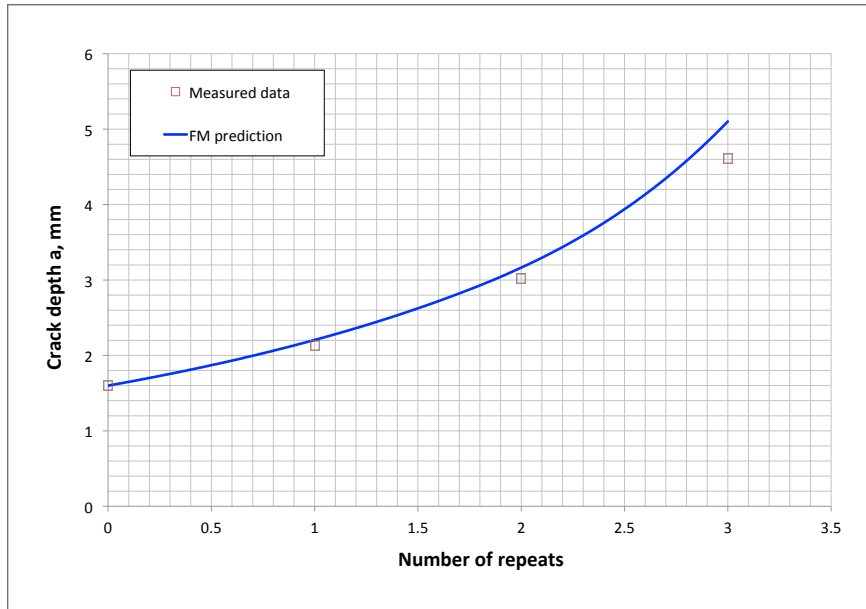


Figure 21 Comparison of fatigue crack growth between experimental measurements and fracture mechanics prediction.

the  $M_k$  curve calculated based on the DNV F101:2013 guidance is still largely below the present  $M_k$  solution for a hi-lo of 1mm. However, a further increase of WRBW to 10mm sees the  $M_k$  curve significantly above the latter.

In the above analysis, only one weld root profile (Type II), with WRBH=hi-lo=0.5mm, was evaluated. In the following, evaluations were also carried out for other types of weld root models for different WRBH and at two different stress levels. The results are summarised in Table 5. The following can be seen from the table:

- For Type I flaws, the fatigue lives calculated based on the current DNV guidance agree well with those calculated by using the  $M_k$  solution developed in this project for high WRBH (1mm in the present example). For smaller WRBH, the current guidance underestimates the fatigue life – a difference of about 22% at a WRBH of 0.25mm;
- For Type II flaws, the predicted fatigue crack growth lives, based on the guidance given in DNV F101:2013, are greater than those calculated based on the present  $M_k$  solution – the difference increased with increasing WRBH

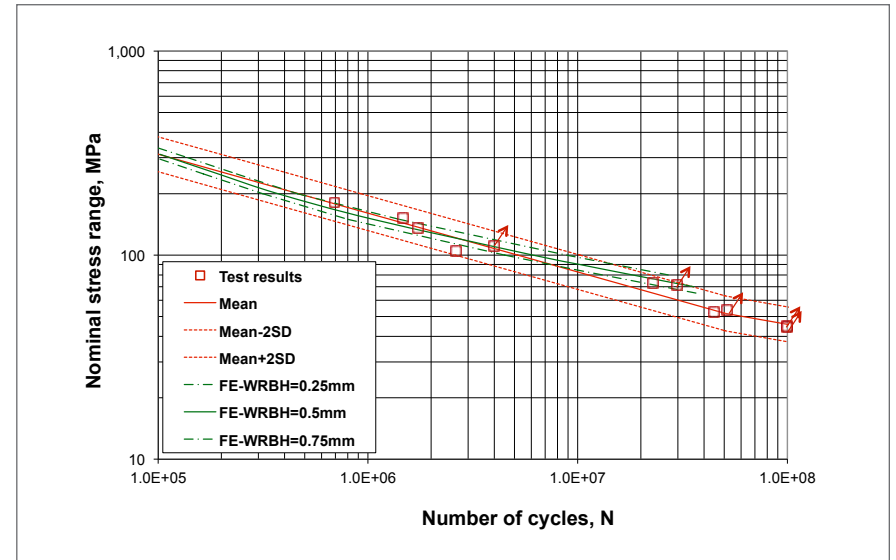
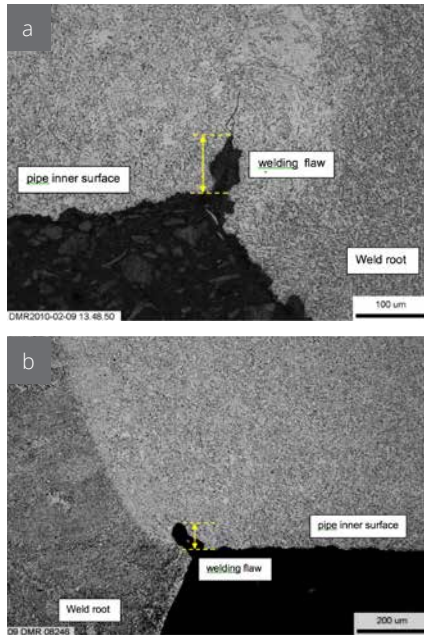


Figure 22 Comparison of the S-N curves, calculated based on fatigue crack growth for type II weld root defect for three different WRBH, with the experimental mean, mean-2SD and mean+2SD S-N curves (Zhang and Maddox, 2014). Those welds, which did not fail, are marked with an arrow.

- (or hi-lo) and decreasing stress level;
- A similar trend was also observed for the Type III flaw models – the difference increased with increasing hi-lo and decreasing stress level. For example, for a weld root with WRBH=1mm, hi-lo=0.75mm, the fatigue life predicted, based on DNV F101:2013 at a stress range 120MPa, is 1.7 times that calculated based on the new FEA-based  $M_k$  solution.

## 8 Discussion

The present analysis indicated that it would be inappropriate to use the existing  $M_k$  solution in BS 7910 to assess a flaw at the weld root bead toe. This is because the existing  $M_k$  solutions were based on models which did not characterise the features of the girth weld root toe. The girth weld root bead width and height are typically small, with w/B and h/B ratios typically ~0.15 and ~0.03 respectively, while they were much greater, with w/B ≥ 0.5 and h/B ≥ 0.1, in the existing  $M_k$  solutions. Furthermore, there is often a step between the weld root bead and the neighbouring pipe surface



**Figure 23** Two examples of the macro-sections, showing the initial welding flaw sizes at the weld root bead toes:  
 a) At W2 weld in pipe S11, flaw depth ~75µm;  
 b) At the girth weld in pipe S26, flaw depth ~68µm.

which could introduce a high SCF at the sudden surface transition location. The misalignment-induced SCF was greater in the present non symmetric model than in the symmetric model where the weld profiles in the weld cap and root were assumed to be identical (Maddox and Andrews, 1990). As a result, the existing  $M_k$  solutions tend to be conservative for Type I defects, but non-conservative for Types II and III defects.

The fatigue performance of girth welds in risers and flowlines strongly depends on the severity of the weld root bead profile. The present analysis indicated that the WRBH, WRBW and hi-lo at the weld root are key parameters influencing the  $M_k$ . Therefore, to improve fatigue performance of girth welds, measures should be taken to control these parameters, especially the hi-lo. Industry is focused on improvement of fatigue performance of risers and flowlines through control of these parameters. Considerable work has been carried out in this area with respect to careful welding parameter control, surface inspection (including laser profilometry), volumetric inspection, control of out-of-roundness at the pipe mill, and by laser measuring and sorting during fabrication.

Although the  $M_k$  solution developed was based on the welds made with a copper backing shoe on the inside surface, it can be conservatively used for assessing defects at weld root with favourable profile, ie, no steps between the weld root and the neighbouring pipe inner surfaces.

The  $M_k$  solution developed in the present project was focused on application to girth welds in risers and pipelines where membrane loading is predominant. The  $M_k$  solution under bending loading was not considered in the present study. Users should therefore exercise caution when applying the new FEA-based  $M_k$  solution to other situations where the proportion of bending

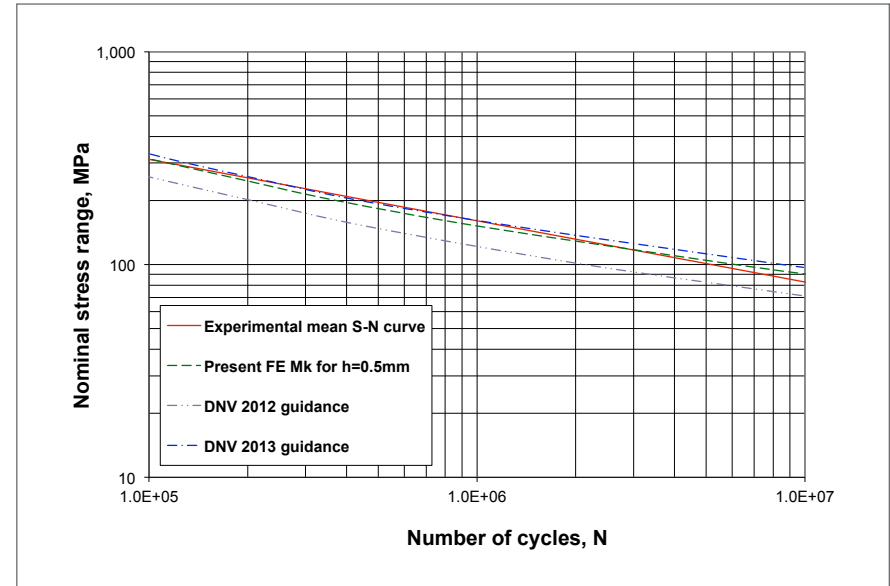


**Figure 24** Comparison of the S-N curves, calculated based on fatigue crack growth, with the experimental results (assuming hi-lo=0.5mm, Type II defect when using the present  $M_k$  solution, and WRBW=3mm when using the BS 7910 2D  $M_k$  solution).

element is significant, eg assessing a flaw at the single-sided weld root in a plate or pipes with high wall thickness. However, comparison of the BS 7910 2D  $M_k$  solutions between axial and bending loading modes, Figure 26, suggests that:

- The difference between the two is negligible for a typical WRBW.
- Use of the  $M_k$  developed under axial loading for cases under bending loading is conservative.

The  $M_k$  solution was developed from a model in which the weld cap was assumed to be ground flush with the pipes and perfectly aligned (no

offset at the weld cap) and the SCF due to the hi-lo at the weld root was included in the solution. If there is a hi-lo at the weld cap, a misalignment-induced SCF due to this hi-lo needs to be considered in the use of the present  $M_k$  solution for assessing a flaw at the weld root bead. If the hi-lo occurs on the same side of the weld as that on the weld root, the misalignment-induced SCF should be included in the assessment, using a method similar to that suggested in BS 7910 (2013). On the other hand, if it occurs on the opposite side of the weld to the hi-lo at the weld root, it would be conservative to ignore this misalignment induced SCF.

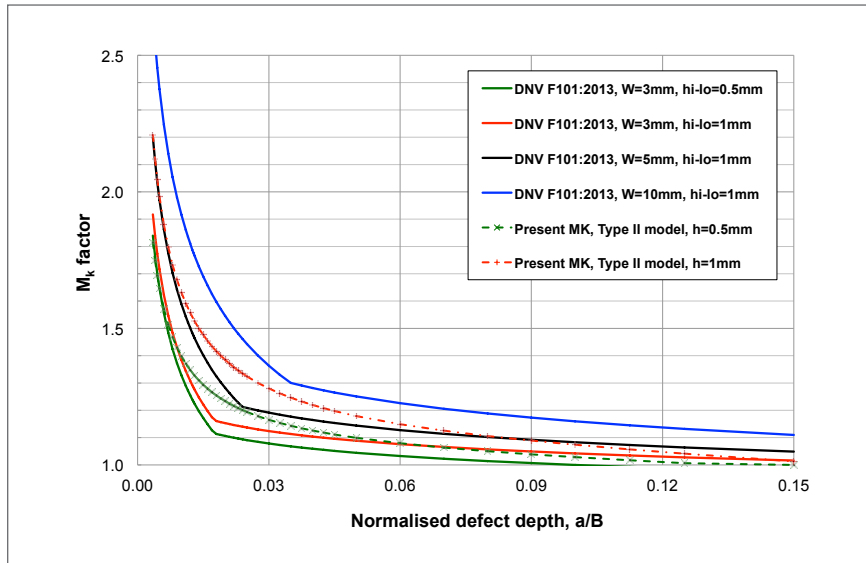


Figure 25 Comparison of  $M_k$  between FEA and BS 7910 2D  $M_k$  solutions, for Type II defect model. For the DNV F101:2013  $M_k$  in the plot, the misalignment-induced SCF was included in those cases where  $hi-lo \neq 0$  in order for comparison with the present  $M_k$  solutions which include the SCF.

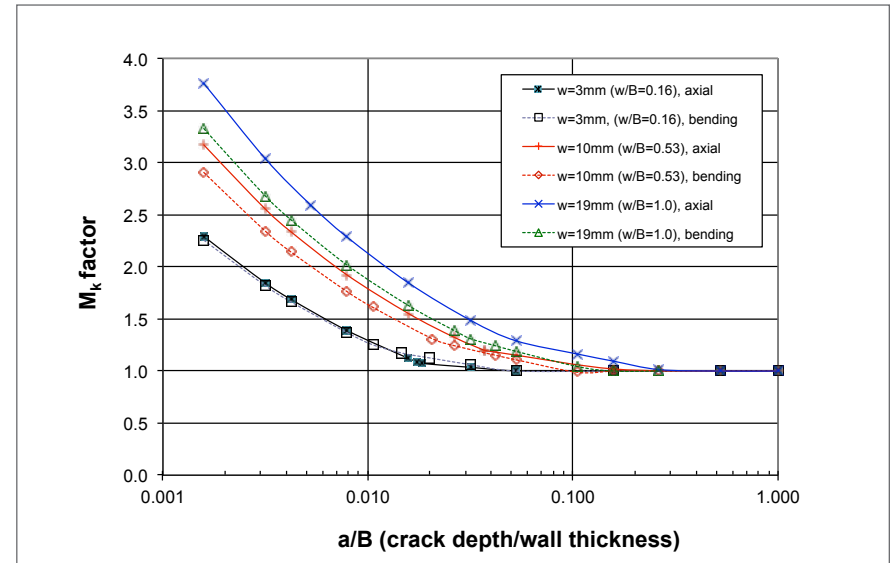


Figure 26 Comparison of the BS 7910 2D  $M_k$  solutions between axial and bending loading modes for three different  $w/B$  ratios (for  $w=3\text{mm}$ , the difference in  $M_k$  between axial and bending loading at  $a/B \sim 0.02$  is likely due to data smoothing).

If the DNV F101:2013 guidance is used to assess a flaw at the weld root toe, the assumed WRBW must be increased to avoid non-conservatism. Cases 3-8 in Table 5 for Types II and III defect models were re-analysed by increasing the WRBW and the results are given in Table 6. It can be seen that it would be conservative to increase the weld width by 3mm for the Type II defect and 2mm for the Type III defect. This simple approach can be applied to weld root profiles with WRBH up to 1mm. Whether this approach can be conservatively used for assessing flaws of all types at the girth weld root toe needs further analysis.

## 9 Conclusions

1. The FE  $M_k$  solutions and the parametric equations for the Type I, II and III defect models have been developed and established.
2. Weld toe angle at the weld root has a negligible effect on the  $M_k$ .
3. The derived  $M_k$  depends on the WRBH at  $w/B > 0.15$ , and on WRBW. For the Type I defect, the  $M_k$  increases with increasing  $w/B$  and  $h/B$ , and eventually reaches a plateau. In all cases analysed, the BS 7910 2D solution provides an upper bound to these curves.

4. For the Type II and III defects, the FE  $M_k$  values are significantly greater than for the Type I defect, and increase sharply with increasing  $hi-lo$ .
5. For the Type III defect, the  $M_k$  solution can be obtained through

the convex combination of the Type I and II defect  $M_k$  solutions.

6. The accuracy of the  $M_k$  solution developed was confirmed by the experimental data in terms of both fatigue crack growth and S-N curve approaches.

7. The guidance given in DNV F101:2012 is unduly conservative for assessing flaws at girth weld roots.

8. The guidance given in DNV F101:2013 predicts fatigue lives comparable with those predicted using the present  $M_k$  solution for relatively small  $hi-lo$  (0.25mm). However, for girth weld roots with greater  $hi-lo$ , the guidance is non-conservative.

9. A simple modification to the current DNV F101:2013 guidance to avoid non-conservatism is proposed, ie, increasing the WRBW by 3mm and 2mm for Type II and III defect models, respectively.

## 10 Recommendation

The  $M_k$  solutions developed in this work, for assessing flaws at a girth weld root toe, should be included in BS 7910.

## 11 Acknowledgements

This work was supported by the Industrial Members of TWI as part of the Core Research Programme.

Some test results from previous funded work were used in the assessment of the accuracy of the  $M_k$  solutions developed. The authors are grateful to the sponsors for permission to use these data: BP Exploration and Production Ltd, Chevron Energy Technology Company, ExxonMobil Upstream Research Company, Heerema Marine Contractors, Petrobras, Saipem SpA, Tenaris Tamsa and the UK Health and Safety Executive.

The authors also thank Dr Isabel Hadley, TWI and Dr Daowu Zhou, Subsea 7, for critical review of the report.

## 12 References

BS 7910:2013+A1:2015 (Incorporating Corrigendum No.1): 'Guide to methods for assessing the acceptability of flaws in metallic structures', British Standard Institution, London, UK.

BS 7608:2014: 'Code of practice for fatigue design and assessment of steel structures', British Standard Institution, London, UK.

Bowness D and Lee M M K, 2002: 'Fracture mechanics assessment of fatigue cracks in offshore tubular structures', HSE Offshore Technology Report 2000/077 for HSE, EPSRC, and Chevron Oil. London: The Stationery Office.

DNV-OS-F101, 2010: 'Submarine pipeline system', October.

DNV-OS-F101, 2012: 'Submarine pipeline system', August.

DNV-OS-F101, 2013: 'Submarine pipeline system', October.

Lotsberg I, 2008: 'Stress concentration factors at welds in pipelines and tanks subjected to internal pressure and axial force', Marine Structures, 21, pp138-159.

Maddox S J and Andrews R M, 1990: 'Stress intensity factors for weld toe cracks', in Proceedings of the conference on Computer Aided Assessment and Control of Localised Damage, 26-28 June, Portsmouth, UK, pp329-342.

Maddox S J, 1991: 'Fatigue strength of welded structures', Woodhead Publishing Ltd.

Maddox S J, 1997: 'Developments in fatigue design codes and fitness-for-service assessment methods',

Performance of Dynamically Loaded Welded Structures, Proceedings, IIW 50th Annual Assembly Conference, San Francisco, Ed: S.J. Maddox, M. Prager. Publ: New York, NY 10017, USA; Welding Research Council, Inc., pp22-42.

Signes E G, Baker R G, Harrison H D and Burdekin F M, 1967: 'Factors affecting the fatigue strength of welded high strength steels', British Welding Journal, 14(3) pp108-116.

Smith I J and Hurworth S J, 1984: 'The effect of geometry changes upon the predicted fatigue strength of welded joints', TWI Research Report 244/1984.

Zhang Y H, Maddox S J and Razmjoo G R, 2002: 'Experimental study and prediction of fatigue crack growth in girth welded pipes', in Proceedings of Offshore Mechanics and Arctic Engineering (OMAE) Conference, Paper No. OMAE 2002-28595.

Zhang Y H and Maddox S J, 2011 : 'Development of fatigue testing of full-scale girth welded pipes under variable amplitude loading', in Proceedings of the 30th OMAE Conference, 19-24 June, Rotterdam, The Netherlands, Paper No. OMAE2011-49942.

Zhang Y H and Maddox S J, 2014: 'Fatigue testing of full-scale girth welded pipes under variable amplitude loading', Journal Offshore Mechanics, Arctic Engineering, 136 (2), pp021401/1-1.



# Technical Literature Reviews



Technical Literature Reviews are a precursor to a project in the Core Research Programme and provide useful subject-related background and references to previously published literature.



## Applications, Modelling and Manufacturing Processes for Perforated Composites

Chris Worrall

Review 25265

### Background

There is a clear industrial need for the development of perforated materials. Perforated metal sheets are used across many industries for a number of applications including blast protection, acoustic damping, aerodynamic tailoring and aircraft anti-icing. Homogeneous metals are relatively easy to machine into these perforated sheets by milling many holes by laser, waterjet, punching or conventional drilling.

Composite materials can offer significant specific property advantages over metals; high stiffness and strength combined with low weight. Their use as perforated panels, however, is yet to be applied in many applications. There are significant difficulties with machining composite materials; the cost of tools to cut the abrasive fibres, and reduction in structural efficiency when fibres are cut. Even with the best quality tools, abrasion quickly becomes a significant problem when drilling large numbers of holes and the tolerances of the holes diminishes, which introduces variability and damage into the parts. Using state-of-the-art machining techniques, such as laser or abrasive waterjet cutting, can reduce the machining problems. Waterjet cutting of composites, however, will require a small initial pilot hole to be drilled in order to eliminate damage, and this is not economical for many small holes (perforations).

For those techniques without this issue there is still the inherent problem that fibres are cut and removed from the composite when making the holes. A greater proportion of the fibres will be cut if a perforated composite is manufactured using this technique, which can significantly reduce the panel's mechanical properties, and as a result additional material must be added, reducing the potential weight savings expected from using the composite.

Cutting a hole in any material reduces its strength, and composites are no exception. A typical carbon fibre composite can suffer tensile strength reduction of up to 35% through inclusion of a single drilled hole (Poon, 1991), although this figure can depend on the composite lay-up. To address this, a recently completed TWI Core Research Project (CRP) successfully developed a new TWI capability to make holes in thermoplastic composites using a novel Thermally-Assisted Piercing (TAP) technique (Brown and Worrall, 2015). The technique offers a process where holes can be machined in thermoplastic composites with reduced detriment to the load-bearing fibres (when compared with current machining techniques). Coupons containing holes made using the TAP process exhibited an improvement in open hole tensile strength of up to 10% compared to coupons with holes made using a conventional drilling/reaming process.

Although originally developed as a precursor to mechanical fastening, it became apparent during the project that wider exploitation opportunities were possible; any application that requires holes to be made in composites. The technique is likely to become more attractive economically when the hole size reduces and the number of holes is increased (perforation) as this is increasingly difficult to achieve in a fast, cost-effective way with conventional machining techniques.

This literature review examines several current and potential applications where perforated composites could be exploited to offer improved performance over similar metal-based structures; anti-icing, sound attenuation, blast protection and joining. Materials of interest are both thermoplastic and thermoset composites; thermoplastics for their potential to be perforated after manufacture, and thermosets for the ease of fibre displacement during perforation before the matrix resin has fully cured. The review also covers simulation of both the process of perforating the composite and the performance of the perforated structure. Finally, a review of competing perforating technologies is included to offer insight into when the Thermally-Assisted Piercing process is most likely to be adopted as a perforating technique for composite structures.

# Technical Literature Reviews



## The Benefits of Preheating for Rotary and Linear Friction Welding

Dick Andrews

Review 30184

### Background

Rotary friction welding is an established industrial joining process which has been used in mass production applications since the mid-1950s. The automotive industry originally adopted this machine-based technology for large volume manufacture of high quality, reproducible solid-state welds, but it is now used for quantity and batch production in a wide range of industries including:

- Automotive
- Construction
- Oil and gas
- Aerospace
- Power generation.

As with all joining processes, there are drawbacks in friction welding, one of which is the surface area of components that can be welded, which is limited to the operating specifications of individual friction welding machines. For example, a large continuous drive rotary friction welding (RFW) machine with

a transmission power of 330kW and a maximum applied force of 1600kN is limited to welding round steel bars with a maximum diameter of 125mm (surface area 12,270mm<sup>2</sup>). Nonetheless, large-scale friction welding machines are in operation particularly in aero-engine manufacture for the production of high value added components. These expensive machines are large with high force capability (~20,000kN (2,000 tons)).

However, as a result of the successful application of the friction welding process (rotary and linear), some current industrial users would like to find a way to increase the capability of their existing friction welding equipment for welding larger surface areas. This requirement, to a certain extent, has been addressed by operators of the alternative solid state welding process, flash butt welding (FBW). An increase in the operating capability of a FBW machine to allow larger sectional areas to be welded than the maximum area quoted in the machine

operating specification is achieved by preheating (PH). The increased temperature of the components to be welded assists the flashing process and reduces the heating and cooling thermal gradients. To date, PH before friction welding has rarely been used in production for:

- Welding higher hardenability steels that are susceptible to cracking
- Scaling up the operating capability of friction welding machines, particularly when welding superalloys, most of which require very high applied welding forces
- Dissimilar material welding where there is a large difference in melting points.

Taking this background information into consideration, a literature review was carried out to ascertain if PH and post weld heat treatment (PWHT) had been considered, or used in friction welding applications.



# PhD Studies





## The Effects of Alumina Purity, Braze Preform Thickness, and Post-Grinding Heat Treatment, on the Microstructure, Mechanical, and Nanomechanical Properties of Alumina-to-Alumina Brazed Joints

Tahsin Kassam, Brunel University

TWI Supervisor, Nicholas Ludford

### Background

Alumina dominates the global advanced ceramics market as it is relatively inexpensive to manufacture and its properties, such as refractoriness, electrical insulation, wear and corrosion resistance, make it suitable for use in a wide range of industrial applications. As a result, alumina has been the most commonly used material in ceramic-to-ceramic and ceramic-to-metal joining studies.

One of the preferred industrial methods for joining dissimilar materials, and specifically ceramics, is brazing. One of the most critical problems in this process is poor wetting of the chemically inert ceramic surface by the braze filler metal. Active metal brazing is a process variant which can be used to overcome these challenges via the inclusion of a highly reactive element, such as titanium, in the braze filler metal composition. Whilst relevant data exists in the literature with regard to active metal brazed joints, there has been relatively little systematic study of these joints and their optimisation.

### Key Findings

The effect of post-grinding heat treatment and Ag-Cu-Ti preform thickness on the strength of alumina-to-alumina-brazed joints made using 96.0 (D-96) and 99.7 (D-100) per cent (by weight) alumina was investigated. Microstructural changes and effects on the hardness distribution in the brazed microstructures were evaluated using nanoindentation. It was found that the post-grinding heat treatment did not affect the surface roughness of either grade of alumina. It did, however, lead to a 5.2% increase in the average flexural strength of D-96 test bars and an 8.4% decrease in the average flexural strength of D-100 test bars. An increase in the braze metal preform thickness, from 50 to 150  $\mu\text{m}$ , led to an increase in the average strengths of D-96 and D-100 brazed joints by 98.3% and 24.0% respectively.

A key finding of the work was that, contrary to the literature, post-grinding heat treatment was observed to degrade the average joint strength of D-96 brazed test bars. The average joint strength decreased from 238 to 106MPa. In addition, the work identified that the use of a lower purity (and lower cost) grade of alumina could potentially result in an increased brazed joint strength compared with the use of a high purity grade.

# PhD Studies



## Multiple Beam Yb:fibre Laser Welding Process for Grade 2205 Duplex Stainless Steel

Maxime Bolut, Brunel University

TWI Supervisor, Jon Blackburn

### Background

This project developed a Yb-fibre laser welding process for Grade 2205 duplex stainless steel with thicknesses of 3 and 6 mm. One important application is the manufacturing of intermediate level nuclear waste containers of these thicknesses. The fibre laser welding process currently used for these containers requires filler wire feed to maintain the microstructure at the weld location. Filler wire adds cost and complexity to the process and has a high failure rate. For this reason, the possibility of removing the requirement for filler wire is very attractive, and one possible way of doing this is to tailor the laser beam's energy distribution delivered to the workpiece to influence the material cooling and therefore the resulting microstructure at the weld location. A tailored energy distribution can be achieved through a multiple beam approach using either a beam splitter module or a diffractive optical element. The project investigated both approaches through a detailed experimental programme.

### Key Findings

An innovative laser welding approach was proposed using a tailored energy beam distribution. Development was performed using duplex stainless steel grade 2205, to improve the weld integrity and eliminate post-weld heat treatment, meeting the stringent requirements for strength and corrosion properties for the nuclear and petrochemical industries. The experimental programme and accompanying analysis have shown that autogenous single beam welding of grade 2205 duplex stainless steel is possible using a slow welding speed, and that the undesirable ferrite volume fraction excess can be reduced by using a tailored energy distribution. A dual beam welding approach with a beam splitter is a practical development tool to find the right energy distribution. A suitable diffractive optical element can be readily integrated with a welding head and can withstand the high power required. The microstructure of the weld can be brought closer to that of the parent material, removing the requirement for a filler wire to be used.

The project has demonstrated that autogenous laser welding, using a multi-beam approach or a diffractive optical component, is capable of reducing the cooling rate and balancing the ferrite-austenite microstructure in order to maintain the material properties. The main benefits from this work include removal of filler material and reducing the complexity of the welding process.



## Multi-Scale Modelling of Hardness Testing

Damaso De Bono, University of Surrey

TWI Supervisor, Tyler London

### Background

Hardness testing and, in particular, nano-mechanical characterisation methods for thin films, metallic coatings and ultra-fine grain material systems, are useful tools for assessing abrasive wear, impact and erosion resistance. However, the highly localised nature of these test methods means that the measurements often exhibit scatter due to anisotropies that occur on length-scales comparable to the volume of material being tested.

To improve test procedures for characterising these material systems, this project developed novel simulation methods for inverse analysis, linking microstructural features to the expected statistical variation in measurements.

### Key Findings

The project involved a combined experimental-numerical programme using:

- Instrumented indentation testing of a range of materials from ultra-fine grain, commercially-pure aluminium to nickel-based superalloys
- Nonlinear, multi-scale finite element analysis incorporating microstructural features
- Detailed metallographic examination of samples.

It has led to:

- A new, robust method for inverse analysis of instrumented indentation testing to recover the tensile properties of tested samples
- A semi-empirical relationship between the expected coefficient of variation of measured hardness and the characteristic length-scale of the microstructure of the test specimen
- Novel homogenisation methods for multi-scale modelling of metals.

This research has provided improved guidance on the limitations of nano-mechanical characterisation techniques as well as the need for data fusion techniques to enhance the interpretation of the test data. Project results have been published in the *International Journal of Mechanical Sciences* and have led to new inverse analysis capabilities at TWI.

# PhD Studies



## Structure-Property Relationships for Protic Ionic Liquids

Joshua Reid, University of York

TWI supervisor: Adam Walker

### Background

Protic ionic liquids (PILs) are an emerging class of liquid materials with a wide variety of potential applications, ranging from fuel cells and electrolytes to metal winning fluids and alternatives to VOC solvents. They are produced by combining an acid and a base to give a liquid salt – with the advantage that the resulting fluid can be ‘tailored’ for a specific purpose, through rational understanding of the effect of the molecular structures of the precursors upon the physicochemical properties of the PIL. One area of application in which PILs are being commercialised is solvent-based recycling. This relies on the use of a solvent designed at the molecular level to selectively dissolve a specific polymer and extract it from a matrix of waste material for onward recycling, facilitating a major increase in the quality and value of the product compared to existing recycling methods. PILs are ideal for this task as they can be rationally designed to be very highly specific – however, such a design-based approach requires a detailed fundamental understanding of how application-relevant properties may be fine-tuned through the choice of the correct molecular structure.

### Key Findings

The project has demonstrated that key physicochemical properties of a PIL, including viscosity, density, vapour pressure and solvation capacity for specific polymers, can all be controlled by rational selection of the functional groups in both the base and acid precursors. These properties are not, as was widely believed at the start of the project, a simple result of the difference in pKa values between the precursors, but result from a complex combination of non-covalent interactions including dispersive (London) forces, permanent and induced dipole-dipole interactions and hydrogen bond donor/acceptor capabilities as well as the degree of ionisation.

- Means of controlling these properties were investigated using a series of similar PILs modified with specific functional groups, including alkyl (R), hydroxyl (OH) and amino (NH<sub>2</sub>) functions.
- The PILs were analysed using a variety of physical (viscometry, refractometry), spectroscopic (NMR, MS, UV-Vis, FT-IR, Raman, XRD, Neutron diffraction) and chromatographic techniques and a series of design rules were generated.
- These rules were demonstrated through the design of a PIL for specific polymer dissolution and recovery of high-purity polymer from mixed waste.
- Additionally, it was demonstrated that both the toxicity and biodegradability of a PIL may be predicted from an interpretation of the relevant properties of the precursors.

The rules established from the experimental work have been consolidated and are being interpreted from the standpoint of statistical thermodynamics and quantum mechanics, with the intention of developing a software-based design tool for task-specific PILs.



## Signal Processing, Image Analysis and Feature Recognition for Long-Range Ultrasonic Testing

Kamran Pedram, Brunel University

TWI Supervisor: Peter Mudge

### Background

Long-range ultrasonic testing is a non-destructive testing technique that employs ultrasonic guided waves for the inspection of large complex structures such as pipes, rods, cable, and rails. A typical system uses an array of ultrasonic transducers to generate an ultrasonic guided wave signal, which propagates through the structure. Discontinuities generate reflections, and the same set of transducers record the returning signal. Knowledge of the speed of the ultrasonic guided wave allows the distance of such discontinuities from the transducer array to be found. Additional information about the location and size of defects can also, in theory, be calculated, but distortion and noise create difficulties in extracting the relevant information from the signal.

### Key Findings

Interpretation of guided wave signals is challenging due to non-ideal propagation of the waves, which degrades the signal to noise ratio and spatial resolution that can be achieved. Signal processing techniques from a range of applications in other technologies were assessed. The signals of interest are usually incomplete, distorted and/or noisy.

The main goals of the work were:

- Identification of smaller defects that cannot be detected due to current noise levels
- Reduction of non-random (coherent) noise
- Increasing the inspection range
- Enhancing the spatial resolution.

An advanced time-frequency signal processing technique, split-spectrum processing, was investigated and developed for ultrasonic applications to enhance signal quality.

The influence of split-spectrum processing filter parameters was assessed, and the parameters optimised to improve signal to noise ratio and spatial resolution. The new technique was compared analytically and experimentally with existing approaches. The split-spectrum processing algorithm increases the signal to noise ratio by an average of 30dB – a substantial improvement. Implementation of the technique will contribute to a significant increase in the capability of guided wave testing, allowing a major increase in the ability to detect defects in structures.

# PhD Studies



## Study of the Impact on Mechanical Properties and Corrosion Resistance of Silica Nanoparticles on a Sol-Gel Based Coating

Laura Vivar Mora, Leeds University

TWI Supervisor, Alan Taylor

### Background

Corrosion of metallic structures can have a significant deleterious impact on the asset, the environment, the economy and even on society. Finding measures to reduce and prevent corrosion damage is crucial. Organic coatings and inorganic coatings have long been used to mitigate corrosion. Combining the best features of both organic and inorganic coatings to create hybrid systems is a significant challenge but is expected ultimately to generate novel coatings with improved performance. This project focused on the identification of preliminary design rules for the integration of functionalised nanoadditives into a polysiloxane coating. A materials-by-design approach was adopted where the impact on the mechanical and electrochemical performance of both the degree of functionalisation applied to the additive and of the loading level was investigated. Silica nanoparticles (27nm diameter) were incorporated into an ethyl silicate based polysiloxane film forming matrix. Surface functionalisation of the silica nanoparticles was undertaken with a propyl epoxy silane at three levels (T0.1, T0.25 and T0.5), where T represents theoretical monolayer coverage. The silica and functionalised silica additives were incorporated into the matrix at three loading levels (10, 15 and 20% by weight).

### Key Findings

The incorporation of non-functionalised silica nanoparticles led to an improvement of barrier properties and mechanical durability of the polysiloxane matrix. Functionalising the surface of the silica particles further improved the corrosion resistance and the mechanical properties of the coatings. This is due to the flexibility introduced into the coating by the propyl epoxy group. In addition, the surface treatment reduced the agglomeration of the silica particles in the coating, leading to a more uniform particle distribution. This, in turn, created an improved barrier to permeation by reducing the defect density and thus contributed to a decrease in the corrosion rate of the underlying substrate. When considering the corrosion resistance and mechanical properties, the coatings which showed the greatest enhancement were those with silica nanoparticles at T0.1 and 20% by weight, followed by the T0.25 and 15% by weight. The relation between the silica nanoparticles, the matrix and the distribution of these nanoparticles through the coating appears to be one of the key factors to improve coating performance. The lowest functionalisation level, T0.1 gave coatings with the best properties overall. This work demonstrated that, with an appropriate nanoparticle functionalisation, silica can be added at loadings up to at least 20% by weight and be homogeneously and uniformly distributed in a polysiloxane matrix. According to these results, we believe that silica at T0.1 could be incorporated at even higher loadings whilst still showing good dispersion. This work has helped to provide fundamental understanding about some of the key factors relating macro-scale performance to nano-scale structures. Whilst many challenges remain in the drive towards commercialisation of these inorganic-organic hybrid coatings, a materials by design approach identifying the key design rules governing behaviour can provide new mechanistic insights, explaining the improved properties of the siloxane coatings after the addition of suitably functionalised nanoparticles.



# Current Core Research Programme Projects

## Materials Characterisation and Performance

- Use of simulated samples to study environmentally-assisted cracking of duplex stainless steel welds
- Effect of microstructure on resistance to hydrogen embrittlement of CRA alloys used subsea
- Damage tolerance of thermal spray aluminium coatings
- Hydrogen embrittlement behaviour of high strength steels
- Corrosion behaviour of wear resistant and corrosion resistant coatings in seawater including the galvanic effect of cathode protection
- Use of thermal spray aluminium to mitigate corrosion under insulation (CUI)
- Evaluation of the microstructure and correlation with properties of cold spray deposited engineering alloys
- Hydrogen-assisted cracking susceptibility of high strength nickel alloys
- Development of a mechanised thermal cycling test facility
- Adhesive-free bond strength test method for cold spray coatings
- Review of recent work on environmentally assisted corrosion (EAC) cracking resistance of duplex stainless steels
- Annular corrosion in flexible pipes
- Evaluation of the effect of key microstructural and environmental parameters on resistance of duplex stainless steels to HISC
- Understanding high pressure/high temperature 'sweet' and 'sour' ( $\text{CO}_2/\text{H}_2\text{S}$ ) environments.

## Joining, Coating and Processing

- Characterisation of modified fibre based composites for enhanced functionality and performance
- Determination of the most appropriate parameters for butt fusion welding PE pipes for maximum long-term integrity of the joint
- Process capability study for friction stir spot welding
- Determination of waisted tensile test energy-to-break factors for different polyethylene pipe resins
- Plasma cathode electron gun
- Robotic friction stir welding
- Linear friction welding of advanced lightweight materials
- Perforated composites
- Development of advanced material modelling for metal additive manufacturing
- Development of ultrashort laser micromachining and surface modification database
- Sulphur corrosion of brazes
- Advancing friction stir welding of thick section aluminium
- Monitoring of arc welding
- Friction stir welding of titanium alloys
- Large scale electron beam welding
- Laser metal deposition for large net shape manufacturing
- LMD surface coating and in-line NDT inspection for wear and corrosion applications
- Initial investigation of arc based additive manufacturing
- Laser cutting of fibre reinforced polymer composites
- The benefits of pre-heating for friction welding
- Assessment of mechanical fastening techniques for dissimilar metals joining in car bodies
- Effect of insufficient homogenisation of pigmented resin during the extrusion of polyethylene pipes on the mechanical performance of butt fusion joints
- Cold atmospheric plasma treatment to enhance joining processes
- Laser welding of crack susceptible materials using tailored energy distributions
- Controlling exposure to hexavalent chromium in welding fume
- Automated process parameter optimisation for robotic arc welding and additive manufacturing
- The properties of similar and dissimilar refill friction stir spot welded joints
- Advancement of wire-fed electron beam additive manufacture
- Hybrid fibre reinforced polymer composite to metal joining.

## Non-Destructive Testing

- Wind turbine blade inspection by shearography
- Customisable phased array boards for intrinsically safe environments
- Determination of the ultrasonic properties of pipeline coatings and mitigation of their effect on guided wave testing
- Quantitative metal loss measurement at contact points using ultrasonic guided waves
- Development of offset X-ray and panel shift computer tomography inspection
- Feasibility of FMC-TOFD for inspection of pipeline girth welds
- Development of early stage creep damage in thermal power plant steels
- Quantitative guided wave inspection techniques for complex tubular structures
- Influencing parameters for the ultrasonic inspection of austenitic welds
- Acoustic emission signal processing for condition monitoring of wind turbine blades
- Advanced signal processing techniques for guided wave inspection of buried pipelines
- Advanced virtual source aperture ultrasound imaging for NDT
- Development of tomosynthesis X-ray inspection techniques
- Automated real time inspection of reduced-pressure electron beam welding.

## Structural Assessment

- Fatigue testing of mooring chain in seawater
- Integrity in aggressive environments: fatigue crack growth behaviour of steel in H<sub>2</sub>S containing environments
- Development of advanced ECA techniques for engineering structures
- Improving the prediction and treatment of residual stresses in ECA
- Development of hierarchical damage mechanics models for predicting strength after impact of composites
- Finite element prediction of stress cycles in mooring chain links under fatigue loading
- Validation of new BS 7910:2013 fracture assessment procedures using full-scale test data
- Fracture resistance behaviour of carbon manganese steel in sour environments.

# Corporate Headquarters and Regional Offices

## Head Office

**TWI Ltd**  
Granta Park  
Great Abington  
Cambridge CB21 6AL  
United Kingdom

Tel: +44 (0)1223 899000  
Email: [twi@twi-global.com](mailto:twi@twi-global.com)  
Web: [www.twi-global.com](http://www.twi-global.com)

## Regional Offices

**TWI Technology Centre North East**  
Ferrous Road  
Riverside Park  
Middlesbrough TS2 1DJ

Tel: +44 (0)1642 216320  
Email: [twinorth@twi-global.com](mailto:twinorth@twi-global.com)

**TWI Technology Centre Yorkshire**  
Advanced Manufacturing Park  
Wallis Way, Catcliffe  
Rotherham S60 5TZ

Tel: +44 (0)114 2699046  
Email: [twiyorkshire@twi-global.com](mailto:twiyorkshire@twi-global.com)

**TWI Technology Centre Wales**  
Harbourside Business Park  
Harbourside  
Port Talbot SA13 1SB

Tel: +44 (0)1639 873100  
Email: [twiwales@twi-global.com](mailto:twiwales@twi-global.com)

**TWI Aberdeen**  
Unit 20 Spires Business Park  
Mugiemoss Road  
Aberdeen AB21 9BG

Tel: +44 (0)1224 691222  
Email: [twiaberdeen@twi-global.com](mailto:twiaberdeen@twi-global.com)

## International Offices

**TWI Azerbaijan**  
World Business Center  
No: 3, Floor: 11  
Intersection S. Vurgun  
& S. Rahimov Str,  
PO Box: AZ1014  
Baku  
Azerbaijan

Tel: +994 12 597 30 33  
E-mail: [training.azerbaijan@twi-turkey.com](mailto:training.azerbaijan@twi-turkey.com)

**TWI Bahrain**  
TWI Gulf WLL  
Suite 52  
Al Saffar House  
Seef  
PO Box 2190  
Manama, Bahrain

Tel: +973 1758 2710  
Email: [qaseemah.malallah@twigulf.com](mailto:qaseemah.malallah@twigulf.com)  
or [sony.mathew@twime.com](mailto:sony.mathew@twime.com)

**TWI Canada**  
TWI Training & Consultancy Ltd  
731 1st Street  
SE Calgary  
Alberta  
Canada T2G 2G9

Tel: +1 403 767 1343  
Mob: +1 587 436 1352  
E-mail: [info@twica.ca](mailto:info@twica.ca)

**TWI China**  
Baliqiaobei Chaoyang District  
Beijing  
PO Box 863  
100024  
China

Tel: +86(0)10 8570 3255  
Web: [www.twichina.com](http://www.twichina.com)  
Email: [enquiries@twichina.com](mailto:enquiries@twichina.com)

**TWI (India) Private Ltd**  
78/97 Chamiers Road  
Nandanam  
Chennai 600-018  
India

Tel: +91 (0)44-43189691/2/3/4  
Email: [enquiries@twiindia.com](mailto:enquiries@twiindia.com)

**TWI Indonesia**

PT. Teknologi Weldim  
Indonesia  
Mutiar Building, 3rd Floor, Room 301  
Jl. Mampang Prapatan Raya No. 10  
Jakarta Selatan, 12790  
Indonesia

Tel: +6221 7942880  
Email: inquiry@twi-indonesia.com  
or rahmadhita@twi-indonesia.com

**TWI Malaysia**

TWI Technology (S.E.Asia) Sdn. Bhd.  
(Reg. No. 247037-X)  
No. 1, Jalan Utarid U5/13  
Section U5, 40150 Shah Alam  
Selangor Darul Ehsan  
Malaysia

Tel: +603 7848 1000  
Email: inquiry@twisea.com

**TWI Pakistan**

257 FF Sector, Commercial Area  
(Next to World Call Office,  
Near FF Club)  
DHA Phase 4,  
Lahore  
Pakistan

Tel: +92(0)-42-36187612/+92(0)-  
308-4443250  
Tel: +92(0)-308-444 3 250/+92-  
(0)-300-4610861  
Email: training@twi-pakistan.com

**TWI Thailand**

TWI Training & Services Co., Ltd  
No. 33/30 Moo,  
1 Sukhumvit Road,  
Naklua, Banglamung  
Chonburi 20150  
Thailand

Tel: +66 (0)38 222136  
Email: inquiry@twi-thailand.com

**TWI Turkey**

Barbaros Mahallesi  
Uphill Towers  
A Block Daire 108  
Atasehir  
Istanbul  
Turkey

Tel: +90 (0) 216 688 4210  
Mobile: +90 (0) 532 693 6108  
Email: ozgur.erdem@twi-turkey.com

**TWI United Arab Emirates**

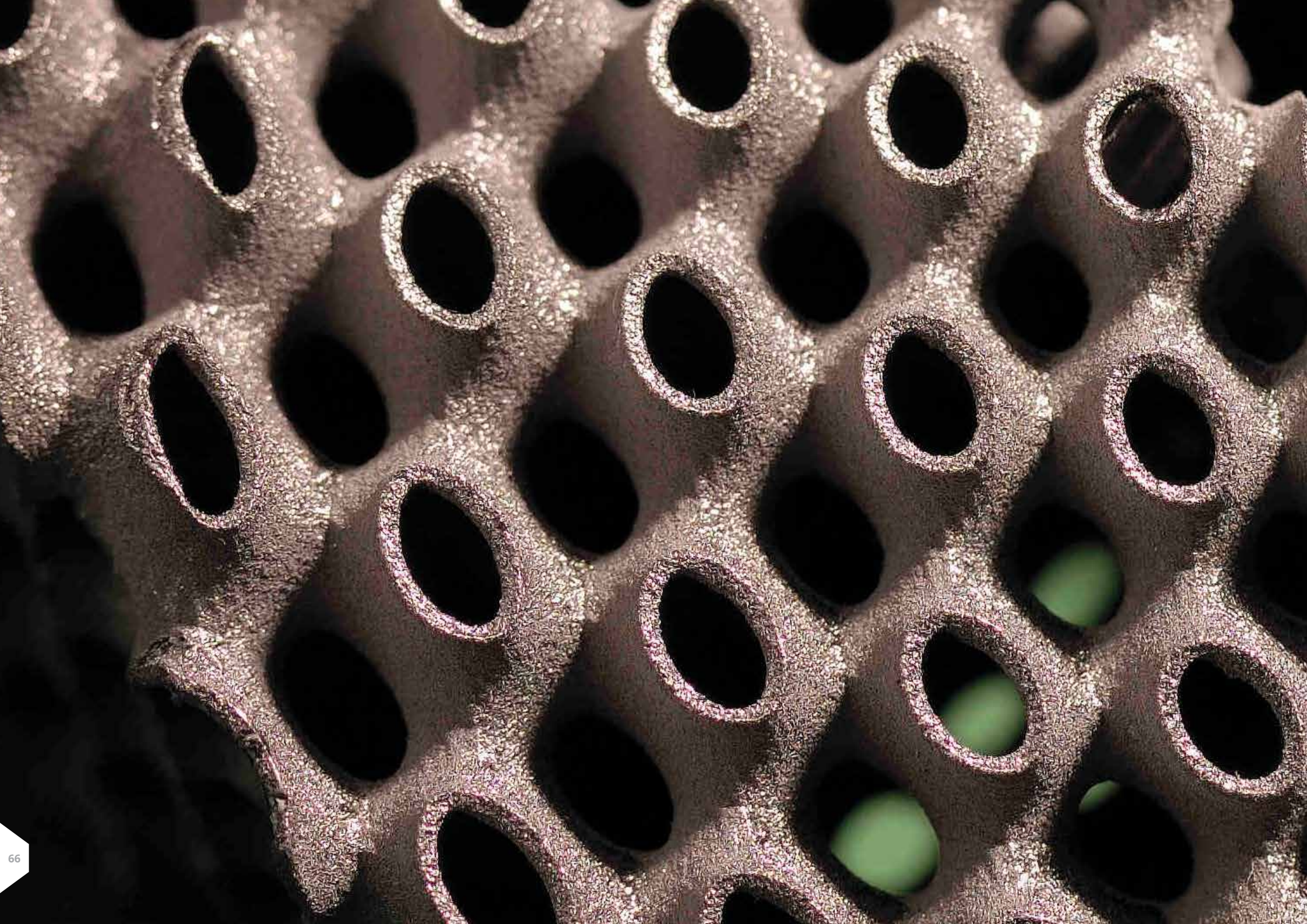
TWI Middle East FZ-LLC  
Knowledge Village  
Block 11  
Offices 101 and 102  
PO Box 502931  
Dubai  
UAE

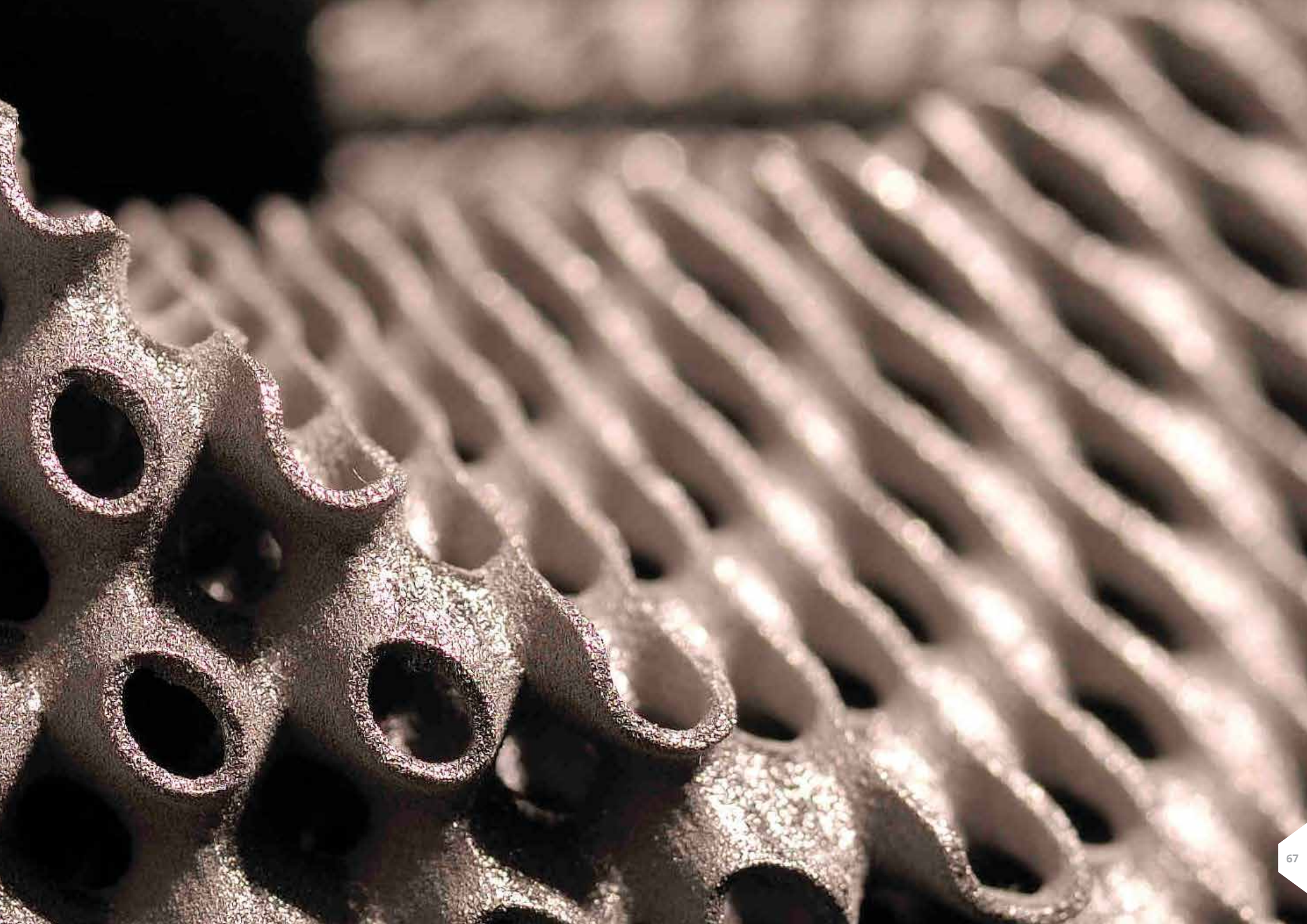
Tel: +971 4 4586657  
Email: deedar.shah@twime.com

**TWI United States of America**

TWI North America, LLC  
12243 C FM 529 Road  
Houston, Texas 77041  
USA

Tel: +1 281 680 2000  
Email: twi@twinorthamerica.com





TWI is the business name of The Welding Institute, a company limited by guarantee.  
The Welding Institute – Registered number 405555 England.  
TWI – Registered number 3859442 England.

[www.twi-global.com](http://www.twi-global.com)